An experimental study of the kinetics of decompression-induced crystallization in silicic melt

Julia E. Hammer and Malcolm J. Rutherford

Department of Geological Sciences, Brown University, Providence, Rhode Island, USA

Received 24 August 2000; revised 6 September 2001; accepted 6 September 2001; published 29 January 2002

[1] Experiments were conducted to study the temporal evolution of feldspar crystallization kinetics during isothermal decompression. Pinatubo dacite was held at 780°C, 220 MPa, f_{O2} = NNO + 2, H_2O-saturated conditions for an equilibration period, decompressed to final pressures, P_f, ranging from 175 to 5 MPa, and then held for 0.3–931 hours. According to the plagioclase liquidus curve in P_{H2O}-T space for the relevant melt composition, these decompressions impose effective undercoolings, ΔT_{eff}, of 34–266°C. Growth of preexisting phenocrysts and newly formed sparse microlites dominate crystallization at $75 \leq P_f < 150$ MPa (ΔT_{eff} = 34–93°C), and equilibrium crystal modes are achieved in <168 hours. Microlite nucleation is the dominant transformation process for $10 < P_f < 50$ MPa (ΔT_{eff} = 125–241°C), and chemical equilibrium is not attained by 168 hours under these conditions. Slow, steady decompressions typically produced normally zoned, euhedral, and planar-faceted feldspar crystals, although anhedral morphologies were produced at very low P_f. Contrary to expectation, slowly decompressed samples were usually further from chemical equilibrium than rapidly decompressed samples after similar durations below the initial pressure. Although counterintuitive, these trends are consistent with new constraints on the relative rates of feldspar nucleation and growth (controlled by ΔT_{eff} and melt viscosity) experienced during each decompression path. Analysis of liquid to solid transformation kinetics using TTT-style diagrams shows that crystallization occurs most rapidly at ~100 MPa by a crystal growth mechanism. The next most efficient crystallization conditions are at 25 MPa, in a crystal nucleation-dominated regime. *INDEX TERMS:* 3630 Mineralogy and Petrology: Experimental mineralogy and petrology, 3640 Mineralogy and Petrology: Igneous petrology, 8434 Volcanology: Magma migration, 8439 Volcanology: Physics and chemistry of magma bodies; *KEYWORDS:* crystallization kinetics, microlites, Pinatubo dacite, textural analysis, crystal nucleation, crystal growth

1. Introduction

[2] Crystallization of a silicate melt during magma intrusion or eruption may result from either a decrease in temperature or a change in the concentration of one of its components. The most common example of the latter is crystallization produced by decompression-induced H_2O loss. Cooling-induced crystallization has been studied in igneous rocks [*Cashman and Marsh*, 1988; *Armienti et al.*, 1994; *Higgins*, 1996a], in laboratory experiments [*Fenn*, 1977; *Swanson*, 1977; *Muncill and Lasaga*, 1987, 1988; *Davis et al.*, 1997; *McCoy and Lofgren*, 1999], and for simple systems with theoretical models [*Hort and Spohn*, 1991; *Granasy and James*, 1998] and is moderately well understood. Kinetic information gleaned from these studies has provided a means of estimating residence times in magma chambers between eruptions [*Mangan*, 1990; *Resmini and Marsh*, 1995; *Higgins*, 1996b]; dating injections and magma mixing events [*Ohnenstetter and Brown*, 1992; *Venezky and Rutherford*, 1997]; calculating solidification rates of dikes, lava lakes, and basalt flows [*Crisp et al.*, 1994; *Cashman et al.*, 1999]; and developing models of magma chamber dynamics [*Solomatov and Stevenson*, 1993; *Simakin et al.*, 1994; *Mourtada-Bonnefoi et al.*, 1999]. However, cooling is not the main driving force for crystallization of ascending H_2O-saturated magmas, which may be nearly isothermal over most of the eruptive sequence [*Wilson et al.*, 1980]. Rather, crystallization induced by an increase in the liquidus temperature as a result of decreasing H_2O concentration in the melt is a more likely driving force in shallow volcanic systems where degassing of ascending magmas is a common phenomenon [*Lipman et al.*, 1981; *Westrich et al.*, 1988; *Stix et al.*, 1993; *Kuritani*, 1999].

[3] Several lines of evidence suggest that extensive groundmass crystallization in response to degassing is not only feasible but is a significant magmatic process occurring within ascending magmas. Experimentally determined phase equilibria in H_2O-saturated systems demonstrate the importance of degassing in the syneruptive crystallization sequence [*Metrich and Rutherford*, 1998], and decompression experiments with Mount St. Helens dacite show that feldspar microlites form on eruptive timescales [*Geschwind and Rutherford*, 1995]. Fluid mechanical models [*Papale and Dobran*, 1994; *Sparks*, 1997; *Melnik and Sparks*, 1999] and observations of volcanic eruptions and their products [*Klug and Cashman*, 1994; *Nakada et al.*, 1995; *Hammer et al.*, 1999; *Nakada and Motomura*, 1999; *Voight et al.*, 1999; *Watson et al.*, 2000] indicate that the processes of syneruptive degassing and magma crystallization can influence eruption dynamics, principally by changing magma rheology.

[4] A promising consequence of magma crystallization in response to degassing is that groundmass textures may preserve valuable information about the decompression path experienced by magmas en route to the surface from crustal reservoirs. Textural attributes such as crystal size and number density are determined by the relative rates of crystal nucleation and growth [*Lofgren*, 1980; *Brandeis and Jaupart*, 1987; *Hort*, 1997; *Roselle et al.*, 1997; *Toramaru*, 2001]. If these crystallization processes can be

0148-0227/02/2001JB000281$09.00

ascribed to degassing conditions such as the depth in conduit where degassing occurs, the degree of supersaturation, and duration of time spent below the magma storage pressure, then groundmass textures may be used to infer ascent dynamics. In turn, knowledge of subsurface magma movement prior to eruption could aid in volcanic hazard assessment and eruption forecasting. One example of an existing petrologic tool for eruption monitoring is the calibrated growth rate of reaction rims on hornblende subjected to conditions outside its stability range [*Rutherford and Hill*, 1993], used for constraining magma ascent rates in the ongoing eruption of Soufriere Hills Volcano, Montserrat [*Rutherford and Devine*, 1997; *Devine et al.*, 1998]. An understanding of the correlation between crystal texture and decompression history, including the functional relationship between the kinetics of crystal nucleation and growth with supersaturation, would extend the range of decompression conditions that can be resolved using crystal textures and allow consideration of magmas that do not contain hydrous phases.

[5] This paper describes laboratory experiments that investigate the kinetics of decompression-induced feldspar crystallization in silicic melt. Our approach differs from previous experimental determinations of crystal nucleation and growth kinetics in several respects: (1) the supersaturation mechanism is devolatilization rather than cooling, (2) the system contains multiple components rather than one, and the liquid to solid transformation involves more than one crystalline phase, (3) no attempt is made to isolate crystal nucleation from crystal growth, as in the traditional two-stage supersaturation approach for nucleation studies [*James*, 1982; *Davis and Ihinger*, 1999] or use of seeded melts for study of crystal growth [*Muncill and Lasaga*, 1987, 1988], (4) decompression experiments begin below the dacite liquidus, so that the starting material contains crystals, and (5) instead of observing the formation and growth of individual crystals through time (as in heating-stage experiments [*Kirkpatrick et al.*, 1979]), multiple experiments run at the same conditions for different durations are used to examine the time evolution of the system. Two independent measurement techniques are employed to monitor changes in crystallinity and texture in the quenched material. These include (1) mass balance to determine the mode of crystal and melt phases and (2) quantitative image analysis of crystal textures to determine rates of kinetic processes. While the chosen approach incorporates more variables and complications than traditional studies of either nucleation or growth from a pure melt, the experiments are intended to approach the complexity of processes as they occur in nature.

[6] Results show that feldspar mode, composition, morphology, and texture depend on the decompression path, degree of supersaturation, and viscosity of the melt during crystallization. Rates of feldspar nucleation and growth are discussed in terms of the balance between effective undercooling generated by decompression and increasing melt viscosity caused by degassing. Finally, progress toward chemical equilibrium is considered in the context of the kinetics of feldspar nucleation and growth. This study is meant to address the kinetics of crystallization in a well-characterized system, the 1991 Pinatubo dacite, with the intention that results will be germane to other silicic magmas.

2. Methods

2.1. Experimental Method

[7] In natural systems, magmas may ascend rapidly as in explosive eruptions, slowly as in effusive eruptions, or at rates that vary as in pulsatory sequences. Experimental decompressions were carried out in two ways: (1) a single drop in pressure followed by an isobaric relaxation interval and (2) 10 steps of equal duration and decompression to final conditions. Single-step isothermal decompression (SSD) from magma chamber conditions to a lower pressure permits examination of a system's response to sudden disequilibration. Textural and compositional evaluation of the products allows the rates of crystallization through crystal nucleation and growth to be determined as simple functions of supersaturation. The decompression paths of the SSD experiments are analogous to those experienced during the 1991 preclimactic events of Mount Pinatubo, Philippines, when magma ascent was arrested at shallow conduit levels for varying amounts of time between explosive pulses [*Hammer et al.*, 1999]. Multistep decompression experiments (MSD) were run to approximate slow, steady decompression. This occurs in nature during dome-forming eruptions, such as the 1995–1998 eruption of Soufriere Hills Volcano, Montserrat, the 1991–1995 activity of Mount Unzen, Japan, and the 1980–1986 dome extrusion at Mount St. Helens, Washington. While steady decompression is one of many viable ascent pathways (accelerating or decelerating decompression may be more likely in natural systems), it is experimentally straightforward and along with the SSD series permits a first-order comparison of the effects of decompression history in determining crystal texture.

[8] The starting material for the experiments was the same lightly crushed phenocryst-rich Pinatubo dacite pumice from the climactic event of the 1991 eruption used to determine preeruptive magma storage zone conditions in the phase equilibrium study of *Rutherford and Devine* [1996]. This is a metaluminous quartz-saturated dacite with a peraluminous (normative corundum of 0.72 wt %) quartz-saturated rhyolite residual melt (Table 1). On a vesicle-free basis the pumice contains 47% phenocrysts, distributed as 31% plagioclase, 12% hornblende, 1% each of cummingtonite, Fe-Ti oxides, quartz, and anhydrite, and trace quantities of biotite, olivine, bronzite, and apatite, as determined by point counts [*Pallister et al.*, 1996]. The remaining 53% is crystal-free glass. Compositions of minerals and glass are given by *Pallister et al.* [1996]. The objective of this study is to characterize the formation and growth of anhydrous phases, primarily feldspar, from the initially crystal-free matrix melt. Changes in the "groundmass," defined here as the matrix melt plus new crystallization in the form of microlites or growth rims on phenocrysts, are the focus of this study. We used lightly crushed material rather than a fine powder to minimize exposure of zoned phenocryst cores to melt and to limit the creation of additional crystal-melt surface area that could enhance crystal growth at the expense of nucleation [*Fokin et al.*, 1999].

[9] Experiments were run in cold seal Waspaloy pressure vessels with nickel filler rods. Hydrothermal pressure was monitored using a pressure transducer checked against a factory-calibrated Heise gauge, with estimated uncertainty of ±1 MPa. The starting material and H_2O sufficient to saturate the melt (7.7 wt % according to solubility model of *Moore et al.* [1995]; typically 10 wt % was added) were placed inside Ag or $Ag_{70}Pd_{30}$ capsules along with unsealed tubes containing a solid oxygen buffer assemblage of Re + ReO_2, which fixed f_{O2} at NNO + 2 [*Pownceby and O'Neill*, 1994; *Evans and Scaillet*, 1997]. When capsules were opened at the end of each run, the presence of both buffer components and liquid H_2O was verified. All charges were held for at least 24 hours at water saturation ($P_{H2O} = P_{TOTAL}$) at 220 MPa (P_i) and 780°C (conditions determined for the preeruption magma reservoir [*Rutherford and Devine*, 1996]) prior to decompression. Charges were then isothermally brought to a range of final pressures (P_f) and held for varying durations before quench (Table 2). Samples were quenched by immersion of the pressure vessel in water and are calculated [after *Carslaw and Jaeger*, 1986] to cool through the glass transition temperature (estimated at two thirds of the liquidus temperature) in ~4.5 s.

[10] In the SSD experiments, decompression times were <4 min, and the instantaneous decompression rate from run to run ranged from 1 to 10 MPa s^{-1}. Samples were maintained at the new pressures for between 20 min and ~931 hours so that the time spent during decompression was in most cases a small fraction of the time spent at P_f. Thus a series of experiments run for different

Table 1. Matrix Glass Compositions of Natural and Experimental Samples

	Pinatubo Natural Climactic Dacite (PR)[a]		
	Pallister et al. [1996]	*Rutherford and Devine* [1996]	P33[b]
Number of analyses *n*	24	6	17
	Microprobe Analyses of Matrix Glass		
SiO_2[c]	76.7(0.8)	76.4(0.2)	71.2(0.4)
TiO_2	0.06(0.03)	0.14(0.04)	0.12(0.03)
Al_2O_3	12.6(0.2)	12.6(0.1)	12.0(0.2)
MgO	0.10(0.02)	0.23(0.03)	0.27(0.03)
CaO	1.20(0.04)	1.28(0.05)	1.42(0.10)
MnO	0.00(0.00)	0.05(0.03)	0.03(0.03)
FeO*	0.74(0.04)	0.79(0.10)	0.79(0.08)
Na_2O	3.66(0.62)	4.10(0.13)	3.71(0.16)
K_2O	3.07(0.20)	2.94(0.05)	2.49(0.05)
Total	98.1(1.0)	98.6	92.1(0.4)
	Analyses Normalized to 100% (Anhydrous Basis)		
SiO_2	78.2	77.5	77.4
TiO_2	0.06	0.14	0.13
Al_2O_3	12.8	12.8	13.1
MgO	0.10	0.23	0.29
CaO	1.22	1.30	1.55
MnO	0.00	0.05	0.03
FeO*	0.75	0.80	0.86
Na_2O	3.73	4.16	4.03
K_2O	3.13	2.98	2.71
	CIPW Norm of Matrix Glass		
Quartz	41.6	38.6	39.7
Corundum	1.1	0.4	0.7
Orthoclase	18.5	17.6	16.0
Albite	31.5	35.2	34.1
Anorthite	6.1	6.4	7.7
Hypersthene	0.7	1.0	1.2
Magnetite	0.5	0.5	0.6
Ilmenite	0.1	0.3	0.3

[a] PR, phenocryst-rich sample (see *Pallister et al.* [1996] for explanation). Parentheses indicate 1σ. Na loss during analysis accounted for on line using method of *Nielsen and Sigurdsson* [1981].

[b] Reference melt for this study, produced with natural climactic dacite, run for 27 hours at 780°C and 220 MPa. Low total is due to dissolved H_2O (solubility at run conditions is 7.7 wt % according to the empirical model of *Moore et al.* [1995]).

[c] FeO* is total iron as FeO.

durations at the same P_f represent "snapshots" of the system through time (Table 2). Experiments with run times of 1 week (168 hours) are also called "series A." The integrated decompression rate (IDR) is defined as the amount of decompression ($\Delta P = P_i - P_f$) divided by time spent below 220 MPa. For MSD experiments this is a constant value: 1.2 MPa h^{-1}, which corresponds to a vertical ascent rate ($\sim$0.015 m s^{-1}) similar to dome-building effusive eruptions [*Rutherford and Gardner*, 2000]. Thus the amount of time spent below P_i varied from 58 to 180 hours in the MSD experiments. Comparison between the products of SSD and MSD decompressions is made using experiments of similar IDR in order to isolate decompression path as an experimental variable distinct from the total crystallization interval duration. The IDRs for series A experiments (0.3–1.3 MPa h^{-1}) are similar to that of the MSD experiments (1.2 MPa h^{-1}). The MSD experiments are hereinafter called "series B."

[11] Several reversal (melting) experiments were run as a check on equilibrium melt compositions and crystal modes. For the reversals, splits of highly crystalline material from long-duration decompression experiments were brought to P_{H2O} of 25, 50, 100, and 150 MPa at 780°C, held for 508 hours, and then quenched.

2.2. Analytical Method

[12] Glasses were analyzed with a Cameca Camebax electron microprobe at Brown University using a 15-kV accelerating voltage, 10-nA beam current, and a defocused beam of 5–15 μm diameter. Sodium was measured first to minimize the effects of its migration, and concentrations were extrapolated to initial (time of 0) values using on-line correction scheme of *Nielsen and Sigurdsson* [1981]. In order to correct for alkali loss in the experimental glasses [*Devine et al.*, 1995; *Morgan and London*, 1996], a suite of Fourier transform infrared (FTIR)-calibrated hydrated glasses were used as "bench" standards. Chips of variably hydrated comenditic obsidian having water contents similar to those of the unknowns were analyzed before and after all experimental glasses. Alkali contents of unknowns were then corrected by factors determined using the bracketing bench standards (as described by *Devine et al.* [1995]). Feldspars were analyzed with a Cameca SX50 at the University of Oregon using the same beam conditions. Microlites ranging in length from 5 to 30 μm were analyzed using the largest appropriate spot size. Only one spot was analyzed on each microlite because of the small crystal size and nominally smaller beam diameter. For zoned microlites the analyses represent the average core compositions.

[13] A multiple nonlinear regression program (Simplex, algorithm of *Albarede and Provost* [1977] provided by M. Baker (personal communication, 1999)) was used to compute the mode of feldspar, quartz, and liquid in each run product using measured feldspar and glass compositions and the glass of P33 (held for 27 hours at the initial conditions; Table 1) as the bulk composition. Thus the groundmass (as defined previously) is treated as a system

Table 2. Decompression Experiments[a]

Run	Type[b]-Series	P_f, MPa	Duration Below P_i, hours	Duration at P_f, hours	IDR,[c] MPa h^{-1}	Fsp, wt %	Qtz, wt %	Total Crystals, wt %	Y,[d] mm s^{-1}	I,[e] mm^{-3} s^{-1}
P31	SSD	220	3	3	0.0	2.3(7.0)	1.8(1.2)	4.1(7.1)	nd	nd
P33	SSD	220	25	25	0.0	0.0(0.0)	0.0(1.2)	0.0(1.2)	nd	nd
P32	SSD-A	220	168	168	0.0	−1.3(6.2)	1.2(1.9)	−0.1(6.5)	nd	nd
P09	SSD	175	167	167	0.3	3.0(5.8)	3.8(1.0)	6.8(5.9)	3.55E-9(1.38E-9)	2.51E-2(1.84E-2)
P53	SSD	150	0.33	0.33	210.0	0.8(7.0)	5.2(1.3)	6.0(7.1)	6.62E-7(3.83E-7)	nd
P22	SSD	150	1	1	70.0	0.4(5.9)	4.7(1.1)	5.1(6.0)	3.63E-7(8.52E-8)	nd
P23	SSD	150	3	3	23.3	3.9(6.5)	4.6(1.2)	8.5(6.6)	1.49E-7(1.71E-8)	nd
P21	SSD	150	27	27	2.6	6.1(6.1)	4.3(1.5)	10.4(6.3)	3.90E-8(7.98E-9)	nd
P42	SSD-A	150	168	168	0.4	15.0(6.7)	6.4(1.3)	21.4(6.8)	5.12E-9(1.24E-9)	nd
P39	SSD	150	931	931	0.1	3.5(11.3)	16.4(2.0)	19.9(11.5)	nd	nd
P70	SSD	150	931	931	0.1	6.0(10.4)	14.3(1.7)	20.2(10.6)	nd	nd
P10	SSD-A	130	167	167	0.5	14.7(8.3)	6.8(3.0)	21.5(8.8)	1.21E-8(2.21E-9)	3.29E-2(2.06E-2)
P30	SSD-A	130	168	168	0.5	15.4(5.7)	7.8(1.1)	23.1(5.8)	9.69E-9(3.49E-9)	nd
P43	SSD	100	0.33	0.33	360.0	4.3(7.8)	3.4(1.1)	7.7(7.8)	1.04E-6(4.48E-7)	nd
P44	SSD	100	1	1	120.0	5.6(7.7)	6.0(1.3)	11.5(7.8)	5.19E-7(2.47E-7)	nd
P45	SSD	100	3	3	40.0	5.8(11.6)	2.5(1.8)	8.3(11.8)	2.65E-7(1.49E-7)	nd
P46	SSD	100	27	27	4.4	7.3(7.8)	7.6(1.1)	14.9(7.8)	3.64E-8(2.16E-8)	nd
P04	SSD-A	100	168	168	0.7	13.0(9.1)	7.3(1.6)	20.3(9.3)	1.34E-8(2.03E-9)	7.74E-2(2.82E-2)
P11	SSD-A	75	168	168	0.9	21.3(5.5)	11.5(1.1)	32.7(5.6)	1.17E-8(2.58E-9)	4.54E-1(2.99E-1)
P52	SSD	50	0.33	0.33	510.0	1.2(4.4)	0.4(1.4)	1.5(4.6)	9.12E-7(2.81E-7)	nd
P24	SSD	50	1	1	172.0	5.9(4.4)	4.7(1.2)	10.5(4.6)	4.63E-7(2.55E-7)	nd
P25	SSD	50	3	3	56.9	7.6(5.8)	5.4(1.3)	13.0(5.9)	2.42E-7(8.79E-8)	nd
P26	SSD	50	27	27	6.3	11.4(4.9)	7.9(1.7)	19.3(5.2)	3.99E-8(4.99E-9)	nd
P13	SSD-A	50	165	165	1.0	16.7(7.1)	7.7(2.9)	24.4(7.7)	1.06E-8(2.03E-9)	6.17E-1(2.17E-1)
P41	SSD	50	931	931	0.2	32.1(7.4)	16.2(1.8)	48.3(7.6)	1.29E-9(2.84E-10)	nd
P06	SSD-A	40	164	164	1.1	34.9(5.2)	20.0(0.8)	54.9(5.3)	6.25E-9(1.62E-9)	1.72E+0(4.13E-1)
P47	SSD	25	0.33	0.33	600.0	7.5(6.8)	3.7(2.5)	11.2(7.3)	1.02E-6(3.96E-7)	nd
P48	SSD	25	1	1	196.6	8.4(6.4)	5.2(2.5)	13.7(6.9)	3.36E-7(1.90E-7)	nd
P50	SSD	25	3	3	65.2	9.3(6.4)	1.9(2.3)	11.2(6.8)	1.90E-7(7.84E-8)	nd
P49	SSD	25	27	27	7.2	28.2(8.5)	17.7(1.7)	45.9(8.7)	2.00E-8(7.92E-9)	nd
P02	SSD-A	25	168	168	1.2	35.3(7.2)	23.7(1.2)	59.0(7.3)	4.93E-9(1.75E-9)	3.81E+0(2.03E+0)
P51	SSD	10	0.33	0.33	629.0	1.9(3.4)	3.4(1.5)	5.3(3.7)	4.58E-7(1.06E-7)	nd
P29	SSD	10	1	1	210.0	8.1(5.9)	5.3(1.4)	13.4(6.0)	3.94E-7(4.00E-8)	nd
P27	SSD	10	3	3	70.0	5.6(10.0)	4.4(2.0)	10.0(10.2)	1.54E-7(2.69E-8)	nd
P28	SSD	10	27	27	7.8	17.4(6.2)	8.2(1.1)	25.6(6.3)	1.86E-8(1.98E-9)	nd
P07	SSD-A	10	164	164	1.3	42.9(5.9)	20.0(1.3)	62.9(6.1)	3.23E-9(4.32E-10)	3.97E+0(1.78E+0)
P40	SSD	10	931	931	0.2	48.0(7.4)	21.7(1.9)	69.7(7.6)	8.48E-10(1.48E-10)	nd
P08[f]	SSD-A	5	164	164	1.3	29.1(2.7)	22.5(1.7)	51.6(3.2)	2.69E-9(6.54E-10)	3.10E-2(9.30E-3)
P38[f]	SSD	5	931	931	0.2	32.1(3.0)	21.4(1.5)	53.5(3.4)	nd	nd
P56	MSD-B	150	58	6	1.2	3.1(5.3)	3.0(1.0)	6.1(5.4)	nd	nd
P57	MSD-B	100	100	10	1.2	6.7(7.0)	4.9(0.9)	11.6(7.0)	nd	nd
P58	MSD-B	75	121	12	1.2	7.8(7.8)	5.5(1.6)	13.3(7.9)	nd	nd
P59	MSD-B	50	142	14	1.2	14.5(5.4)	9.4(1.2)	24.0(5.6)	nd	nd
P67	MSD-B	25	162	16	1.2	14.8(8.6)	9.5(1.1)	24.3(8.7)	nd	nd
P68	MSD-B	10	175	18	1.2	16.3(8.0)	10.2(1.5)	26.5(8.2)	nd	nd
P69	MSD-B	5	179	18	1.2	43.6(2.7)	25.1(0.9)	68.7(2.8)	nd	nd
P63	reversal[g]	150	508	508	0.0	5.7(1.0)	4.3(4.9)	10.0(5.0)	nd	nd
P62	reversal	100	508	508	0.0	17.9(1.2)	9.6(13.4)	27.4(13.5)	nd	nd
P61	reversal	50	508	508	0.0	33.8(7.7)	15.6(1.6)	49.4(7.8)	nd	nd
P60	reversal	25	509	509	0.0	nd	nd	100.0	nd	nd

[a] Values in parentheses, 1σ uncertainty in calculated wt % crystal content based on analytical errors propagated through mass balance calculation; nd, not determined. Read 1.38E-9 as 1.38×10^{-9}.
[b] SSD, single-step decompression to final pressure (P_f); MSD, multistep decompression.
[c] Integrated decompression rate: ΔP_{TOTAL}/experiment duration.
[d] Feldspar microlite growth rates (Y) represent average (and 1σ) values calculated for the 10 largest observed crystals.
[e] Feldspar microlite nucleation rates (I) represent average (and 1σ) values calculated from several images.
[f] Uncertainity in the crystal mode likely to be greater than indicated due to the effects of phenocryst resorption on bulk composition.
[g] Reversal experiments brought to P_f immediately using P38 and P40 as starting material.

that does not exchange mass with existing phenocrysts. The calculation was made using SiO_2, K_2O, CaO, Na_2O, and Al_2O_3 as components, which comprise ≥99.5 wt % of the normalized anhydrous glasses. Using initial estimates for the mode (obtained from linear least squares regression), Simplex propagates analytical uncertainty through a nonlinear regression in order to assign 1σ error bars to each modal value (Table 2). One inherent flaw in this simple mass balance assessment is that phenocryst dissolution or reaction (e.g., breakdown of hydrous minerals) could occur as a result of changing equilibrium phase relations during decompression. Thus the bulk liquid composition would change due to mass exchange with phenocrysts and not be included in the calculations. These effects are mitigated to some extent by two factors: (1) Coupled cation diffusion of NaSi and CaAl in feldspar, the dominant phenocryst phase, is extremely sluggish [*Smith and Brown*, 1988]. As a consequence, feldspar equilibration with melt often occurs by means of growth of a new layer rather than by cation exchange with the melt. Furthermore, crystallization, not dissolution, of feldspar is the expected result of decompression at H_2O-saturated conditions [*Tuttle and Bowen*, 1958; *Blundy and*

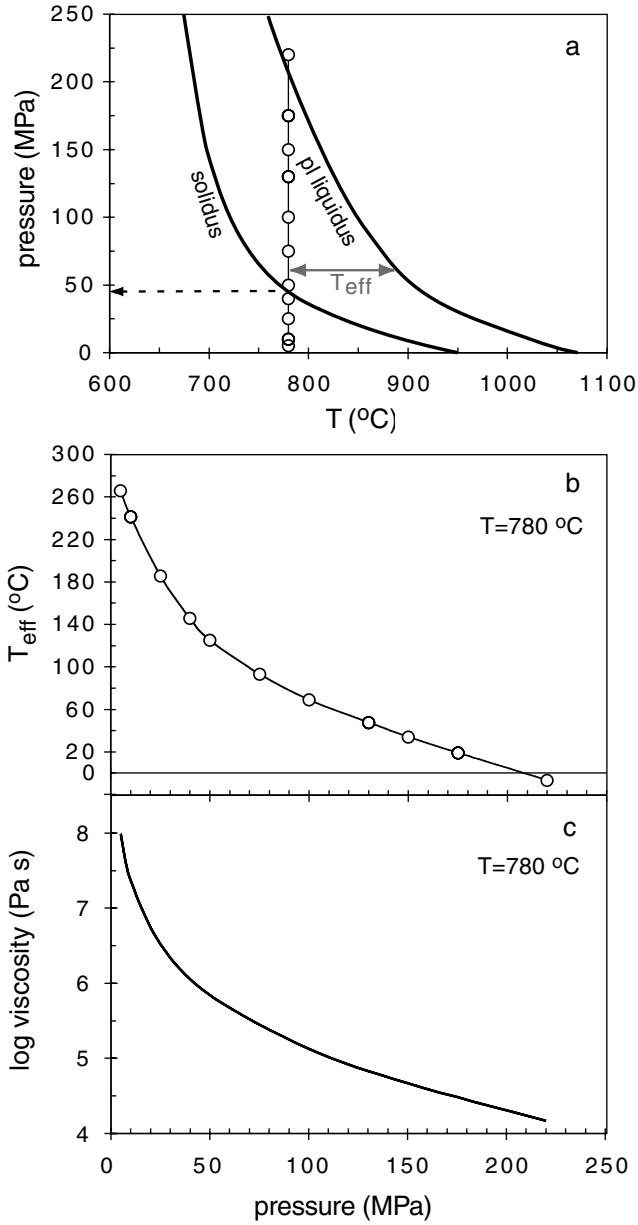

Figure 1. (a) Plagioclase liquidus and the solidus as derived from available experimental data. ΔT_{eff} is defined at any given pressure as liquidus temperature minus 780 (°C). Circles represent experimental pressures in SSD experiments used in this study. Dashed line shows solidus pressure used to define the crystallization interval (see text). (b) ΔT_{eff} as a function of pressure showing experimental conditions (circles). (c) Viscosity of reference melt calculated using the formulas of *Hess and Dingwell* [1996] and *Moore et al.* [1995].

Cashman, 2001]. (2) Hydrous minerals did not form reaction textures in any of these experiments, even after prolonged exposure to P_{H2O} far below stability conditions. Apparently, hornblende, biotite, and cummingtonite breakdown reactions are effectively inhibited by reaction kinetics at the low temperature of the experiments (780°C).

2.3. Image Analysis

[14] The starting material contains intrinsic heterogeneities such as crystal fragments and vapor bubbles, and additional grain surfaces were introduced by crushing in the preparation of experimental charges. Thus we can reasonably assume that heterogeneous nucleation of feldspar occurs [*Berkebile and Dowty*, 1982]. However, we did not observe container-initiated crystallization as described in previous studies employing synthetic starting materials [*Klein and Uhlmann*, 1974; *Swanson*, 1977; *Granasy and James*, 1998], so in this sense, all the observed microlites are "internally" nucleated. Furthermore, the matrix of the starting material is an optically clear glass; any faceted feldspar crystals <30 μm in the experimental groundmass had to nucleate during the experiment. For these small crystals, identification of primary growth surfaces (e.g., facets, dendrites, and swallowtail protrusions) and the lack of compositional unconformities are the main criteria used to distinguish microlites from phenocryst fragments. For larger crystals the distinction based on compositional zoning patterns and perimeter morphology is more difficult, and uncertainties in textural measurements increase commensurately.

[15] Polished thin sections of experimental run products were imaged using backscattered electrons (BSE) with a Cameca SX50 microprobe at the University of Massachusetts, Amherst, and a JEOL6300 scattering electron microscope (SEM) at the University of Oregon. Images were acquired from at least five regions of each thin section to average over existing spatial heterogeneity in texture. The area fraction microlites (ϕ_m) and microlite number density (number mm^{-2}, N_A) were obtained using methods from *Hammer et al.* [1999]. From these measurements, estimates of characteristic crystal size, s_n [mm] = $(\phi_m/N_A)^{1/2}$, and volumetric number density, N_V [mm^{-3}] = N_A/s_n, were calculated. The N_V calculation is based on the standard method for correcting for the cut effect in the stereological conversion of area to volumetric density [*Cheng and Lemlich*, 1983].

[16] A time-integrated nucleation rate, I [mm^{-3} s^{-1}], was then calculated using N_V and the time (t) each sample spent below 220 MPa as $I = N_V/t$. The maximum value of growth rate, Y, was determined for the 10 largest microlites in each sample: $Y = (LW)^{0.5}/(2t)$, where L and W are the measured lengths and widths, respectively. This determination of maximum growth rate is analogous to that reported in previous experimental studies [*Fenn*, 1977; *Swanson*, 1977] and thus is preferred over the bulk-averaged quantity. (Multiplying these values by a factor of 2 allows comparison with reported measurements obtained using

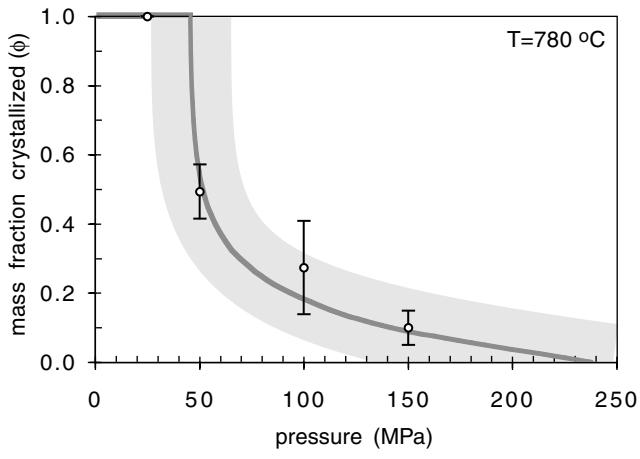

Figure 2. Equilibrium crystallization curve with estimated uncertainty (shaded) as a function of pressure derived from *Whitney* [1988]. Fraction crystallized (ϕ) refers to the experimental groundmass, where $\phi = 0$ at 238 MPa (liquidus) and $\phi = 1$ at 45.5 MPa (solidus) at 780°C. Four reversal experiments using completely crystallized starting material are shown (circles) for comparison.

the entire crystal length [e.g., *Klein and Uhlmann*, 1974]. Caveats to these expressions arise because both quantities are time-averaged over the experiment duration. Both I and Y are minimum values if a lag time exists between decompression and the onset of crystal nucleation.

[17] The methods used in this study afforded the opportunity to characterize a greater number of samples than would be feasible using traditional crystal size distribution (CSD) analysis, which requires hundreds of measurements of individual crystals and a stereological correction for their three-dimensional aspect ratio [*Higgins*, 1994; *Peterson*, 1996]. It has been shown that the bulk methods outlined above give similar results to detailed CSD analysis [*Hammer et al.*, 1999] for tabular microlites growing in response to a single supersaturation event. Since the third dimension of hopper, swallowtail, and bladed morphologies cannot be determined using two-dimensional measurements as it can for tabular crystals [*Higgins*, 1994], it is not clear how CSDs should be corrected to reflect noneuhedral forms.

3. Effective Undercooling and Equilibrium Crystal Mode

[18] Analysis of the present kinetic data requires determination of the position of the plagioclase liquidus as a function of P_{H2O} at 780°C and an estimate of the equilibrium crystal content for each P_f. Appropriate melt and plagioclase liquidi were determined using experimental data from this and early studies of the granite system [*Tuttle and Bowen*, 1958; *James and Hamilton*, 1969; *Johannes*, 1984; *Johannes and Holtz*, 1996]. Constraints on the phase relations in the system Ab-Or-An-Q-H_2O at 100 MPa are provided by an investigation of the shift in liquidus surface and reaction curves with varying An content [*James and Hamilton*, 1969]. The liquidus temperature for the composition of our reference melt (P33) is constrained by the An_{10} isobaric phase diagram at 100 MPa to lie between 825 and 850°C [*James and Hamilton*, 1969, Figure 6]. A second observation was the appearance of plagioclase as a groundmass phase between 220 and 175 MPa in the present experiments, yielding an interpolated plagioclase liquidus pressure of 208.5 MPa at 780°C. Combining these data with the assumption that the curvature of the liquidus with decreasing P_{H2O} parallels that of the plagioclase liquidus in the haplogranite system [*Tuttle and Bowen*, 1958], the plagioclase liquidus curve is estimated for this system (Figure 1a). The effective undercooling, ΔT_{eff}, for each decompression is defined as the difference between the equilibrium feldspar liquidus temperature and the run temperature (780°C) at a given pressure (Figure 1b). Because of the change in slope of the feldspar liquidus curve, ΔT_{eff} increases rapidly as a function of pressure below 50 MPa. At the lowest pressure examined, 5 MPa, the melt is subject to ΔT_{eff} = 266°C. This is higher than previous estimates of effective undercooling imposed by decompression of H_2O-saturated rhyolite melts (175°C [*Westrich et al.*, 1988] and 200°C [*Swanson et al.*, 1989]).

[19] The position of the solidus was determined using available experimental data. *Johannes* [1984] investigated the addition of Ca-plagioclase on the granite solidus at 200 and 800 MPa. At these conditions the solidus shifts from the haplogranite minimum to higher temperatures with increasing An content. However, in the presence of An_{20} plagioclase the solidus is only ~4.5°C greater than the haplogranite solidus. The normative An content of the reference melt is 7.7 wt %, so the solidus at 780°C for this composition is negligibly different from that of H_2O-saturated haplogranite, which occurs at 45.5 MPa. Quartz is present as a phenocryst phase in the starting material, and the extrapolated quartz liquidus pressure based on observed modes at 780°C is 238 MPa. Therefore the total crystallization interval for the reference melt at the experimental temperature is estimated to be 238–45.5 MPa.

[20] Granitic, H_2O-saturated melts do not crystallize linearly with undercooling or decompression. Crystallization intervals for the standard R4 granite superimposed on T-X_{H2O} phase diagram [*Whitney*, 1988 Figure 3b] show that each tenth of melt transformed corresponds to halving of pressure in the liquidus-solidus interval. This form of the crystallization path was rescaled to the reference melt crystallization interval to estimate the equilibrium crystal fraction of the dacite groundmass as a function of pressure. This estimate of the equilibrium crystallization path is in agreement with the results of four reversal experiments (Figure 2).

4. Results

[21] Crystallization of quartz, feldspar, and other phases in minor abundances occurred in all decompression experiments, either in the form of microlite formation, phenocryst growth, or mineral-melt exchange reactions. Groundmass phases exhibit a spectacular variety of textures (Figures 3–5), with complementary changes in melt and crystal chemistry. These changes are caused by three experimental variables: final pressure, duration at final pressure, and decompression path to the final pressure (Table 2). The effects of time and pressure on melt and crystal compositions, microlite textures, and nucleation and growth kinetics are presented in the following sections. Within each section, the results are given first for the series A experiments, which show the effects of ΔP at a given snapshot in time after decompression (Figure 3). Next, the corresponding series B (MSD) runs are described (Figure 4). Finally, results are presented for the remainder of the SSD experiments, which track changes through time at several different P_f (Figure 5).

4.1. Melt Composition and Crystal Mode

[22] Matrix glass compositions were obtained for all experiments in which the groundmass crystallinity of the sample was ≤70% (Table 3). Irrespective of decompression history, the sum of groundmass quartz and feldspar obtained from mass balance calculations is linearly correlated to the melt K_2O content (Figure 6), since K_2O is effectively incompatible with respect to precipitating phases over much of the crystallization interval. The lack of inflection at alkali feldspar saturation (at ~5 wt % K_2O) is interpreted to reflect its low mass fraction of the total crystallizing assemblage.

[23] Melt compositions and crystal modes of the matrix are shown as a function of pressure for series A in Figure 7. With a change in pressure from 220 to 150 MPa, melt SiO_2 increases by 2 wt % due to crystallization of plagioclase, quartz, and minor amounts of oxide and pyroxene. The proportion of feldspar to quartz steadily increases during this interval, until plagioclase and quartz crystallize in a ratio of ~2:1, causing SiO_2 to plateau at ~79.0 wt % between 150 and 50 MPa. With the saturation of alkali feldspar at ~50 MPa, melt K_2O content levels out at just over 5 wt %. Between 50 and 40 MPa the abundance of both quartz and feldspar doubles, and a slight increase in the proportion of quartz causes a drop in melt SiO_2. Despite this increase, crystallinity at 40 MPa is below the equilibrium value. Between 40 and 10 MPa, overall crystallinity increases only slightly. Interestingly, the total crystallinity of the 5-MPa experiment is less than that of the 10-, 25-, or 50-MPa runs (Figure 7e) despite having experienced far greater ΔT_{eff} (Figure 1). This is primarily an expression of inadequate feldspar crystallization (Figure 7c), and BSE images show partial resorption of plagioclase phenocrysts in this experiment (Figure 3f) The uncertainty associated with the mass balance calculation of crystal mode in this experiment is greater than in other samples.

[24] Another view of melt composition evolution in response to crystallization at varying P_f is obtained by projecting these matrix glass compositions onto the haplogranite (Qtz-Ab-Or) ternary diagram and accounting for small normative An content in the melts using the method of *Blundy and Cashman* [2001]. The progression toward Qtz of the feldspar + quartz cotectic with

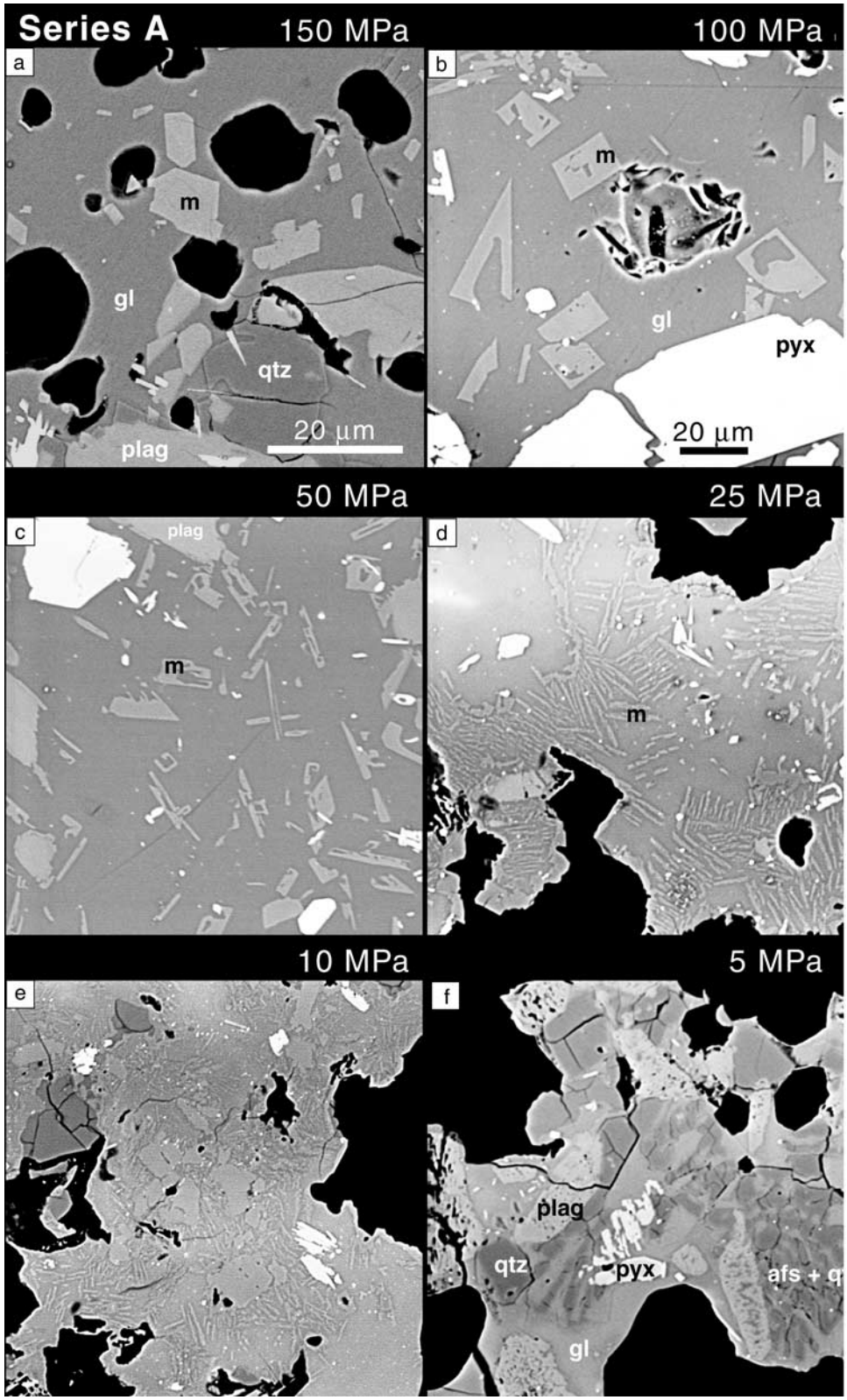

Figure 3. (a–f) BSE images of series A SSD experiments (168 hours at P_f) for various P_f. White, mafic minerals; light gray, plagioclase feldspar (m, microlites); medium gray, glass; dark gray, quartz; black, vesicles, pits, and cracks. At large P_f (>125 MPa), microlites are euhedral and subequant (Figure 3a). With decreasing P_f, crystals display hopper (Figure 3b), swallowtail (Figure 3c), and chain morphologies (Figures 3d and 3e) and are increasingly abundant. At very low P_f, intergrown quartz and alkali feldspar grow at the expense of plagioclase phenocrysts, plagioclase and pyroxene phenocrysts react with melt, and microlites do not form (Figure 3f). Scale bar in Figure 3b applies to Figures 3b–3f.

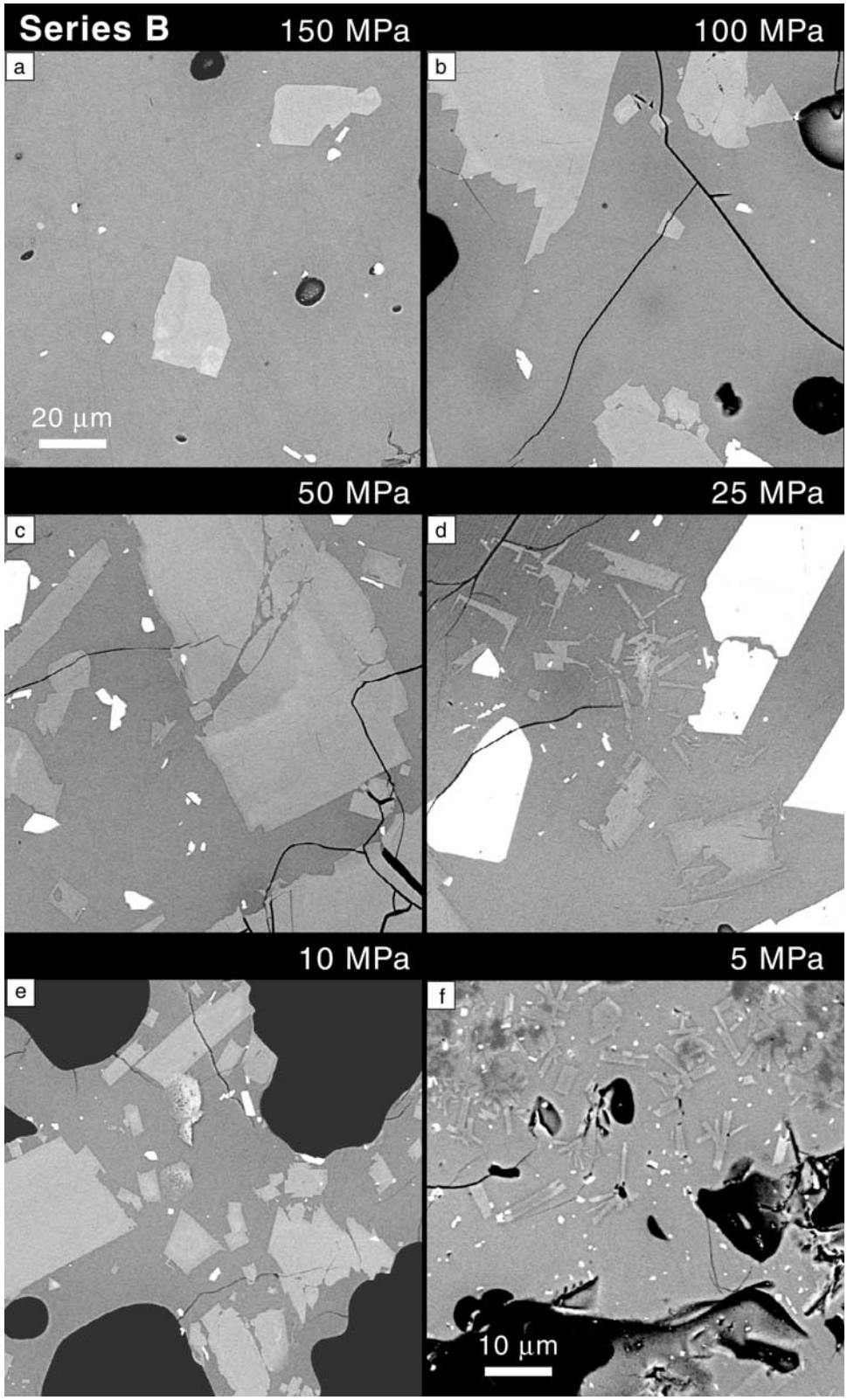

Figure 4. (a–f) BSE images of series B MSD experiments at varying P_f. The decompression rate of all experiments is 1.2 MPa h^{-1}; run duration increases with decreasing P_f (see text). At all $P_f > 5$ MPa, crystallization occurs primarily as growth rims and protrusions on plagioclase phenocrysts. Note zoned skeletal groundmass crystals (Figure 4d). At $P_f = 5$ MPa, plagioclase microlites with lighter alkali feldspar tips form in isolation and in clusters with interstitial quartz (darker gray, anhedral), presumably during the final decompression steps. Scale bar in Figure 4a applies to Figures 4a–4e.

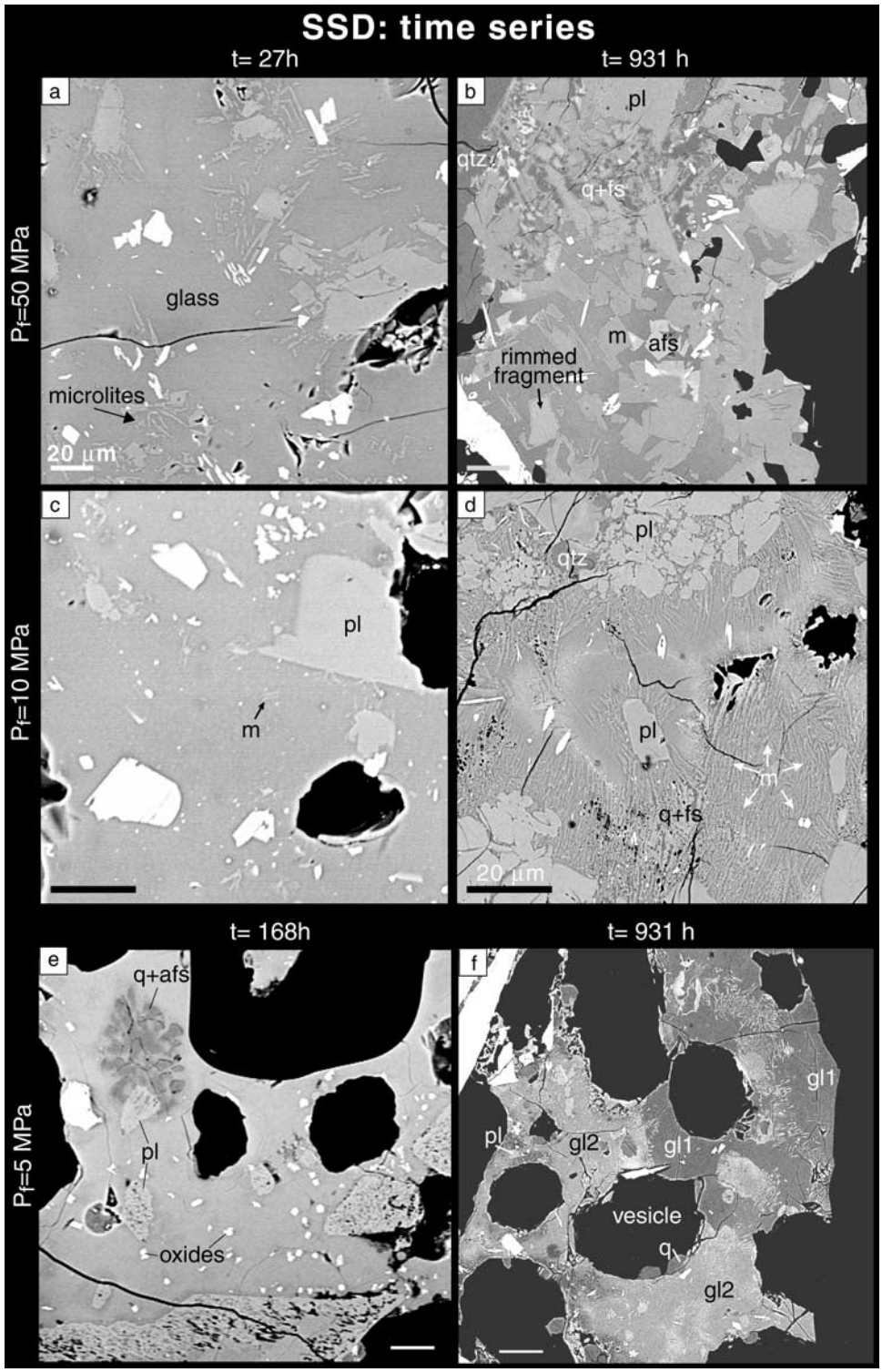

Figure 5. (a–f) BSE images for time series SSD experiments with P_f = 50, 10, and 5 MPa. White, mafic minerals; black, vesicles and pits in sample surface; light gray, feldspar, including plagioclase phenocrysts (pl), plagioclase microlites (m), and alkali feldspar (afs). At 50 MPa, microlite occurrence changes with time from isolated, high aspect ratio cellular crystals (Figure 5a) to blocky, intergrown, and rimmed aggregates (Figure 5b). At 10 MPa, thready sparse microlites (Figure 5c) evolve to a dense network of laths or blades intergrown with quartz (Figure 5d). Plagioclase resorption and oxide crystallization characterizes the early stage at 5 MPa (Figure 5e), followed by intense crystallization of albitic plagioclase, alkali feldspar, and quartz at longer times (Figure 5f). Inhomogeneous matrix, ranging from K-rich (gl1) to Na-rich (gl2) compositions (see Table 3), are identified by gray scale variation in the groundmass. All scale bars are 20 μm.

Table 3. Experimental Matrix Glass Compositions[a]

	SSD Experiments							
	P31	P33	P32	P09	P53	P22	P23	P21
P_f [t][b]	220[3]	220[25]	220[168]	175[167]	150[0.33]	150[1]	150[3]	150[27]
Total[c]	92.01	92.08	92.78	93.24	92.14	93.99	94.49	94.50
n	9	17	6	9	9	8	8	9
SiO_2	77.4(0.3)	77.3(0.4)	76.8(0.2)	77.0(0.2)	76.1(0.5)	76.2(0.1)	77.1(0.4)	77.6(0.3)
TiO_2	0.13(0.06)	0.13(0.03)	0.15(0.05)	0.14(0.03)	0.16(0.04)	0.16(0.02)	0.12(0.02)	0.10(0.05)
Al_2O_3	12.9(0.1)	13.1(0.2)	13.4(0.2)	13.1(0.1)	13.5(0.3)	13.6(0.1)	13.0(0.2)	12.8(0.2)
MgO	0.24(0.02)	0.29(0.03)	0.33(0.01)	0.21(0.03)	0.25(0.01)	0.21(0.02)	0.16(0.03)	0.15(0.02)
CaO	1.35(0.08)	1.54(0.11)	1.57(0.10)	1.34(0.05)	1.68(0.07)	1.58(0.06)	1.33(0.07)	1.19(0.05)
MnO	0.04(0.03)	0.03(0.03)	0.04(0.05)	0.07(0.05)	0.04(0.04)	0.02(0.02)	0.04(0.05)	0.03(0.02)
FeO*	0.81(0.12)	0.86(0.10)	1.07(0.10)	1.01(0.05)	1.03(0.16)	1.09(0.11)	0.89(0.08)	0.78(0.08)
Na_2O	4.28(0.22)	4.04(0.16)	4.10(0.10)	4.24(0.16)	4.34(0.17)	4.36(0.14)	4.36(0.15)	4.20(0.15)
K_2O	2.84(0.07)	2.71(0.06)	2.54(0.17)	2.88(0.06)	2.88(0.09)	2.83(0.07)	2.98(0.08)	3.09(0.13)
	SSD Experiments							
	P42	P39	P70	P10	P30	P04	P43	P44
P_f [t][b]	150[168]	150[931]	150[931]	130[167]	130[168]	100[168]	100[0.33]	100[1]
Total[c]	92.52	94.54	94.01	93.24	92.26	91.95	93.67	94.66
n	8	10	10	8	8	8	8	8
SiO_2	78.9(0.4)	75.0(0.4)	76.0(0.3)	78.4(1.1)	78.8(0.4)	77.7(0.7)	77.1(0.3)	76.3(0.4)
TiO_2	0.09(0.04)	0.17(0.05)	0.12(0.04)	0.15(0.04)	0.11(0.04)	0.14(0.05)	0.11(0.04)	0.16(0.05)
Al_2O_3	12.3(0.2)	13.8(0.2)	13.3(0.2)	12.0(0.5)	11.9(0.3)	12.3(0.4)	13.0(0.2)	13.1(0.2)
MgO	0.16(0.02)	0.11(0.02)	0.09(0.02)	0.16(0.09)	0.09(0.02)	0.17(0.01)	0.21(0.02)	0.21(0.03)
CaO	0.95(0.07)	0.66(0.05)	0.73(0.06)	0.81(0.11)	0.93(0.12)	1.14(0.08)	1.53(0.07)	1.75(0.05)
MnO	0.05(0.03)	0.04(0.02)	0.04(0.03)	0.07(0.05)	0.04(0.03)	0.05(0.05)	0.04(0.04)	0.03(0.04)
FeO*	0.63(0.08)	1.07(0.08)	0.96(0.08)	0.78(0.11)	0.77(0.10)	1.10(0.05)	0.90(0.08)	0.99(0.10)
Na_2O	3.57(0.09)	5.71(0.20)	5.33(0.22)	3.71(0.21)	3.82(0.12)	4.03(0.26)	4.16(0.16)	4.43(0.23)
K_2O	3.42(0.09)	3.45(0.05)	3.46(0.06)	3.92(0.40)	3.48(0.07)	3.33(0.17)	2.93(0.07)	3.01(0.08)
	SSD Experiments							
	P45	P46	P11	P52	P24	P25	P26	P41
P_f [t][b]	100[3]	100[27]	75[168]	50[0.3]	50[1]	50[3]	50[27]	50[931]
Total[c]	93.89	95.30	95.97	92.08	94.35	93.45	94.88	95.11
n	6	9	8	7	8	8	8	9
SiO_2	77.8(0.2)	76.9(0.4)	78.6(0.5)	77.2(0.4)	77.0(0.3)	77.2(0.3)	77.0(0.3)	79.9(1.7)
TiO_2	0.11(0.04)	0.14(0.03)	0.12(0.06)	0.13(0.04)	0.14(0.06)	0.13(0.03)	0.15(0.05)	0.12(0.04)
Al_2O_3	12.8(0.2)	12.9(0.3)	12.1(0.3)	13.2(0.2)	13.1(0.2)	13.0(0.2)	13.1(0.2)	11.1(0.3)
MgO	0.20(0.02)	0.17(0.01)	0.10(0.02)	0.36(0.04)	0.20(0.02)	0.17(0.03)	0.18(0.03)	0.05(0.53)
CaO	1.32(0.07)	1.29(0.09)	0.71(0.07)	1.56(0.08)	1.54(0.10)	1.48(0.08)	1.38(0.15)	0.35(0.53)
MnO	0.03(0.04)	0.06(0.03)	0.02(0.02)	0.02(0.03)	0.05(0.03)	0.04(0.04)	0.05(0.03)	0.04(0.04)
FeO*	0.76(0.10)	1.00(0.12)	0.80(0.04)	0.91(0.12)	0.92(0.06)	0.80(0.07)	1.01(0.07)	0.59(0.44)
Na_2O	3.98(0.18)	4.35(0.15)	3.68(0.22)	3.90(0.10)	4.02(0.12)	4.05(0.21)	3.87(0.16)	2.98(0.23)
K_2O	3.03(0.17)	3.19(0.07)	3.86(0.10)	2.69(0.08)	2.97(0.08)	3.08(0.09)	3.24(0.18)	4.86(0.31)
	SSD Experiments							
	P13	P06	P47	P48	P50	P49	P02	P51
P_f [t][b]	50[165]	40[164]	25[0.33]	25[1]	25[3]	25[27]	25[168]	10[0.33]
Total[c]	93.12	95.38	92.23	91.99	94.96	91.27	97.74	93.71
n	11	5	9	8	8	8	4	10
SiO_2	78.4(1.1)	78.4(0.3)	77.4(0.3)	76.9(0.5)	78.1(0.3)	77.9(0.2)	77.0(0.1)	77.0(0.4)
TiO_2	0.15(0.04)	0.12(0.05)	0.12(0.03)	0.13(0.03)	0.14(0.04)	0.09(0.02)	0.10(0.06)	0.14(0.03)
Al_2O_3	12.0(0.5)	12.0(0.3)	13.1(0.1)	13.4(0.3)	12.5(0.2)	12.7(0.1)	12.9(0.1)	13.3(0.2)
MgO	0.16(0.07)	0.09(0.02)	0.25(0.03)	0.29(0.03)	0.19(0.02)	0.12(0.05)	0.14(0.02)	0.22(0.02)
CaO	0.85(0.17)	0.45(0.06)	1.58(0.09)	1.71(0.07)	1.50(0.06)	0.88(0.12)	0.57(0.08)	1.44(0.09)
MnO	0.06(0.04)	0.04(0.05)	0.05(0.04)	0.02(0.02)	0.05(0.03)	0.03(0.03)	0.04(0.04)	0.03(0.03)
FeO*	0.79(0.13)	0.59(0.08)	0.92(0.09)	0.99(0.09)	0.91(0.09)	0.69(0.07)	0.78(0.08)	0.82(0.04)
Na_2O	3.70(0.19)	3.08(0.11)	3.83(0.16)	3.91(0.16)	3.78(0.14)	3.24(0.18)	3.16(0.10)	4.15(0.23)
K_2O	3.91(0.40)	5.29(0.10)	2.77(0.10)	2.72(0.14)	2.76(0.03)	4.35(0.14)	5.26(0.13)	2.92(0.11)
	SSD Experiments							
	P29	P27	P28	P07	P40[d]	P40[d]	P38[d]	P38[d]
P_f [t][b]	10[1]	10[3]	10[27]	9[164]	10[931]	10[931]	5[931]	5[931]
Total[c]	93.12	95.05	91.34	97.75	99.11	99.70	91.62	99.11
n	9	8	6	5	2	8	9	3
SiO_2	76.5(0.3)	76.8(0.7)	77.2(0.3)	77.3(0.2)	76.7(0.2)	77.9(0.4)	77.6(0.8)	79.6(2.0)
TiO_2	0.18(0.05)	0.15(0.02)	0.16(0.04)	0.13(0.03)	0.14(0.03)	0.12(0.04)	0.11(0.02)	0.06(0.02)
Al_2O_3	13.2(0.3)	13.2(0.3)	13.0(0.2)	12.5(0.2)	13.0(0.0)	13.3(0.2)	13.0(0.3)	12.2(1.1)
MgO	0.23(0.03)	0.27(0.02)	0.17(0.03)	0.21(0.03)	0.00(0.00)	0.02(0.02)	0.21(0.17)	0.02(0.01)
CaO	1.59(0.07)	1.59(0.23)	1.48(0.10)	0.45(0.11)	0.53(0.09)	2.58(0.58)	0.27(0.10)	1.49(0.42)
MnO	0.05(0.04)	0.03(0.03)	0.02(0.02)	0.08(0.04)	0.00(0.00)	0.04(0.05)	0.08(0.04)	0.03(0.02)

Table 3. (continued)

	SSD Experiments							
	P29	P27	P28	P07	P40[d]	P40[d]	P38[d]	P38[d]
FeO*	1.18(0.11)	0.91(0.14)	0.84(0.13)	0.99(0.08)	0.17(0.05)	0.22(0.06)	0.97(0.40)	0.16(0.09)
Na_2O	4.12(0.14)	4.15(0.25)	3.88(0.11)	2.91(0.16)	3.30(0.32)	4.41(0.33)	2.83(0.39)	4.32(0.90)
K_2O	2.90(0.10)	2.96(0.17)	3.25(0.06)	5.40(0.15)	6.08(0.62)	1.40(0.86)	4.90(0.33)	2.09(0.51)
	SSD Experiment	MSD Experiments						
	P08	P56	P57	P58	P59	P67	P68[d]	P68[d]
P_f [t][b]	5[164]	150[58]	100[100]	75[121]	50[142]	25[162]	10[175]	10[175]
Total[c]	98.15	92.82	94.36	93.67	96.28	96.73	92.55	92.31
n	3	8	8	8	9	8	6	4
SiO_2	75.4(0.2)	77.4(0.3)	77.5(0.4)	77.6(0.7)	77.8(0.5)	77.6(0.2)	78.0(0.4)	79.7(0.2)
TiO_2	0.17(0.05)	0.11(0.03)	0.16(0.03)	0.14(0.03)	0.10(0.03)	0.12(0.03)	0.15(0.04)	0.12(0.05)
Al_2O_3	13.6(0.2)	13.1(0.1)	12.7(0.3)	12.7(0.4)	12.6(0.3)	12.8(0.2)	12.5(0.2)	11.6(0.2)
MgO	0.21(0.06)	0.22(0.03)	0.22(0.02)	0.20(0.03)	0.10(0.01)	0.13(0.02)	0.09(0.02)	0.09(0.02)
CaO	1.10(0.13)	1.26(0.05)	1.25(0.08)	1.22(0.09)	0.91(0.08)	0.97(0.06)	0.75(0.05)	0.59(0.02)
MnO	0.06(0.02)	0.04(0.03)	0.05(0.04)	0.04(0.03)	0.05(0.03)	0.03(0.03)	0.06(0.03)	0.06(0.04)
FeO*	1.03(0.21)	0.86(0.07)	0.83(0.09)	0.82(0.12)	1.03(0.04)	0.96(0.09)	0.76(0.08)	0.68(0.07)
Na_2O	3.27(0.18)	4.09(0.18)	4.13(0.12)	4.16(0.17)	3.97(0.17)	3.83(0.10)	3.95(0.15)	3.62(0.09)
K_2O	5.11(0.39)	2.88(0.04)	3.07(0.02)	3.16(0.13)	3.48(0.11)	3.51(0.12)	3.76(0.20)	3.51(0.07)
	MSD Experiment	Reversal Experiments						
	P69	P63	P62	P61				
P_f [t][b]	5[179]	150[508]	100[508]	50[508]				
Total[c]	97.13	93.45	94.01	93.57				
n	10	8	5	5				
SiO_2	77.6(0.4)	77.4(0.2)	78.4(0.8)	78.1(0.9)				
TiO_2	0.14(0.06)	0.15(0.05)	0.14(0.06)	0.09(0.04)				
Al_2O_3	11.8(0.3)	12.9(0.1)	12.0(0.4)	12.3(0.6)				
MgO	0.25(0.11)	0.23(0.02)	0.11(0.01)	0.13(0.08)				
CaO	0.29(0.05)	1.15(0.03)	0.91(0.19)	0.66(0.24)				
MnO	0.06(0.03)	0.03(0.03)	0.04(0.03)	0.04(0.04)				
FeO*	1.09(0.19)	0.93(0.06)	0.77(0.07)	0.60(0.07)				
Na_2O	2.96(0.17)	4.25(0.07)	3.95(0.25)	3.49(0.16)				
K_2O	5.74(0.12)	2.96(0.06)	3.68(0.08)	4.57(0.24)				

[a] Electron microprobe analyses of matrix glasses normalized to 100 wt % (anhydrous basis). FeO* is total iron as FeO. Parentheses indicate 1σ.
[b] P_f, final pressure (MPa); [t], duration at P_f (hours).
[c] Sum of oxide wt % prior to normalization. Totals <100% are attributed primarily to dissolved H_2O.
[d] Matrix in highly crystalline samples is inhomogeneous (see Figures 5b, 5d, and 5f). The first of the two analyses corresponds to the dark matrix in BSE images and was used in the mass balance calculation of feldspar and quartz crystallinity (Table 2).

decreasing P_{H2O} in the H_2O-saturated system [*Tuttle and Bowen*, 1958; *Holtz et al.*, 1992] has been used to track the crystallization pressures of natural magmas during ascent [*Cashman and Blundy*, 2000]. During equilibrium crystallization the normative melt composition records the closure pressure (P_c), at which kinetic factors inhibit chemical equilibration. Experimental samples undergoing moderate decompressions ($P_f \geq 40$ MPa) show equilibrium liquid lines of descent produced by cotectic feldspar and quartz precipitation (Figure 8a). For these runs the melt composition indicates closure pressure near the experimental pressure ($P_c \approx P_f$); in fact, the melt in the 40-MPa experiment achieved the minimum composition for this pressure and temperature. Decompressions to lower P_f produced melts that progressively diverge from this path. Instead, these melts indicate enrichment of the Ab component and $P_c \gg P_f$. Relative to quartz and alkali feldspar, plagioclase crystallization was insufficient for the melt to progress along an equilibrium path toward the appropriate cotectics.

[25] Samples decompressed in stepwise fashion experienced a very different crystallization history than the SSD runs (Figures 7 and 8b). Although feldspar and quartz increase gradually with decreasing P_f, lower melt concentrations of SiO_2, K_2O, and CaO in all runs with $P_f > 50$ MPa reflect lower feldspar and quartz contents than in the SSD runs. The crystallinity contrast between SSD and MSD samples dramatically reverses at $P_f = 5$ MPa. Whereas the feldspar crystallization was inhibited in the SSD experiment (Figure 7c), an abrupt increase in both feldspar and quartz contents occurs in the MSD run (Figure 7d), bringing its total crystallinity to the maximum observed value among all runs of similar duration (Figure 7e). In contrast to series A, $P_c > P_f$ for all series B experiments, not just for $P_f < 50$ MPa (Figure 8b). However, unlike the low P_f series A runs, the trend in melt composition with decreasing P_f is consistently away from the Ab component in series B. The jump in crystallinity of the series B 5-MPa experiment results in a melt composition that is much closer to equilibrium than the corresponding series A run.

[26] The time evolution of melt composition and relative proportions of feldspar and quartz in SSD experiments is shown for several P_f in Figure 8c. At $P_f = 50$ MPa, melts attain the appropriate cotectic in 168 hours by crystallization of albitic feldspar ($P_c = P_f$). However, instead of proceeding down the cotectic toward the minimum composition at this pressure, the melt overshoots the cotectic and moves into the quartz field due to insufficient quartz crystallization (or overproduction of feldspar) at 931 hours. The 10- and 5-MPa sequences both show inhibited feldspar relative to quartz, and both trends in melt composition change course between 168 and 931 hours. At 10 MPa, melts progress toward the low-pressure cotectic by crystallizing quartz and feldspar (although in a different proportion than in the 50-MPa series), but upon nearing the 50-MPa cotectic, an increase in the quartz crystallization relative to feldspar causes the melt to move away from equilibrium, toward the Or component (K_2O-rich glass; Table 3). In the 5-MPa series, plagioclase feldspar crystallization is even more sluggish initially (as shown in the resorption textures of

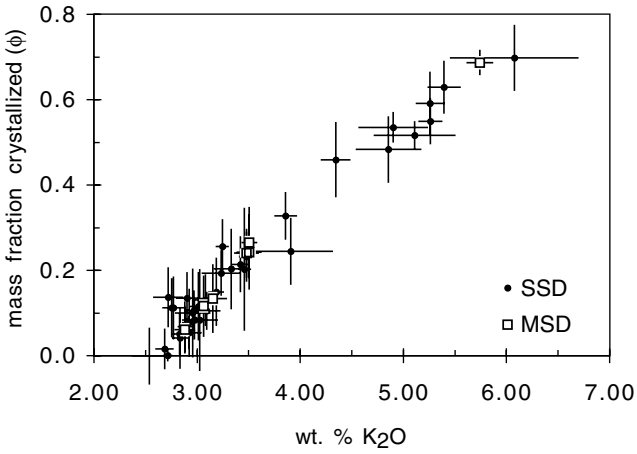

Figure 6. Melt K_2O content (recalculated anhydrous) versus groundmass crystallinity (the sum of quartz and feldspar from mass balance).

Figure 5e), driving the melt toward Or (and $P_c \gg P_f$). By 931 hours, crystallization of plagioclase and alkali feldspars has brought the melt to the 50-MPa cotectic ($P_c > P_f$). Both of the low-P_f, long-duration samples contain inhomogeneous matrix (Figures 5d and 5f), with compositions falling into two groups, (1) high K2O and Al2O3 and (2) high Na2O and CaO. The latter is interpreted to be a very fine intergrowth of quartz, feldspar, and glass. This texture has been observed in effusively erupted material from Mount St. Helens [*Cashman*, 1992; *Blundy and Cashman*, 2001].

[27] The time series data are also considered in terms of the approach to equilibrium crystal concentration. Because each experiment with $P_f \geq 47.5$ MPa is approaching a different equilibrium crystallinity (Figure 2), the observed crystallinities are scaled by the equilibrium crystal content at each P_f (either the maximum observed crystal content for that pressure or an estimate based on Figure 2). The resulting normalized crystal content, X, represents the fractional approach toward equilibrium (Figure 9). The scaled trends are essentially log linear and similar in slope within uncertainty (average slope of 0.093 h^{-1}; 1σ = 0.006), with the crystallization onset time as the only significant difference among time series. The largest decompressions ($P_f \leq 50$ MPa) were relatively slow to begin crystallizing and never achieved more than 70% of the equilibrium values. In contrast, substantial progress toward equilibrium ($X = 0.3-0.4$) was made in under 1 hour for $P_f \geq 100$ MPa.

4.2. Feldspar Compositions

[28] Feldspars grown in decompression experiments range from An_{53} plagioclase to Or_{64} alkali feldspar, with more evolved

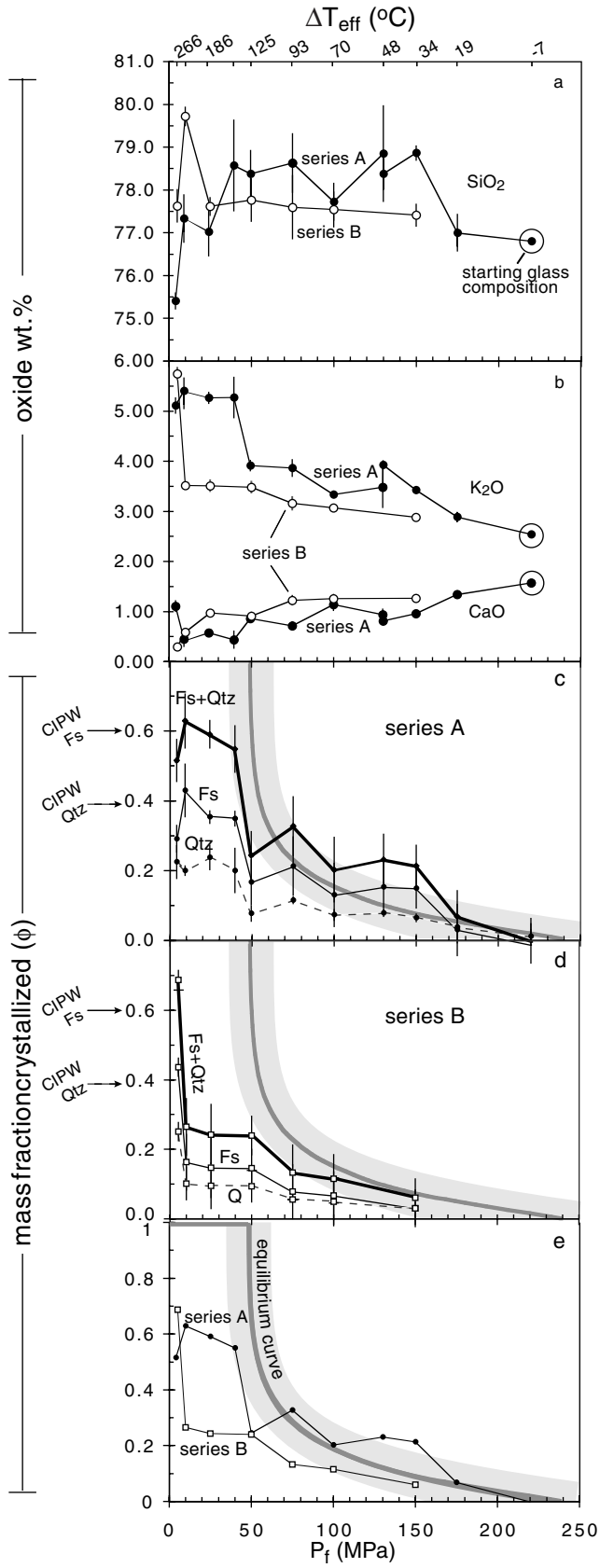

Figure 7. (opposite) (a and b) Recalculated anhydrous melt compositions: series A (single step decompressions), solid symbols; and series B (multistep decompressions), open symbols. Circled points at 220 MPa represent the starting melt used to compute modes by mass balance. Error bars are 1σ of multiple analyses. Mode of feldspar (Fs) and quartz (Qtz) determined by mass balance for (c) series A and (d) series B experiments with the CIPW normative values of the starting melt for comparison. The 1σ error bars represent propagation of analytical uncertainty through the calculation. Error associated with 5 MPa run is likely to be larger than indicated due to partial resoption of plagioclase phenocrysts. (e) The sums of Qtz and Fs for both series shown with the estimated equilibrium curve (see text and Figure 2). Error bars are omitted for clarity.

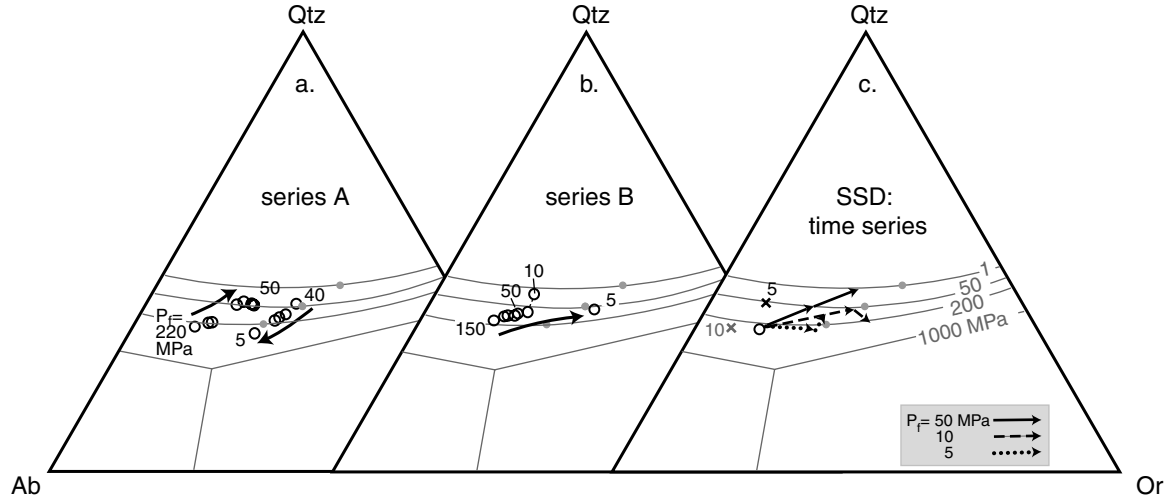

Figure 8. Matrix glass compositions projected onto haplogranite ternary [*Blundy and Cashman*, 2001] showing liquid lines of descent in comparison with H_2O-saturated cotectic curves and minimum compositions (gray dots). (a) Series A. Arrows point toward decreasing values of P_f for separate SSD experiments and do not indicate the paths taken by the melt during decompression. The actual paths taken by melts begin at point labeled P_f = 220 MPa and end at each circle symbol. Below 40 MPa, plagioclase crystallization is increasingly inhibited as indicated by reversal of the trend back toward Ab. (b) Series B. Arrows point toward decreasing values of P_f as for Figure 8a. There is no reversal in trend at low P_f, although below 50 MPa the melt composition does not reflect equilibrium crystallization. Inhomogeneous matrix compositions (connected with dotted line; see Table 3) in the 10-MPa experiment straddle the 50 MPa cotectic. (c) Time series SSD. First arrow segment indicates direction of melt evolution during first 168 hours following decompression, and second segment represents the path during the 168- to 931-hour interval. The 10- and 5-MPa samples have inhomogeneous matrix compositions; analyses suspected to represent fine-scale crystalline intergrowths are shown as labeled crosses.

compositions occurring in highly crystallized samples. Feldspar compositions observed in series A experiments are compared with series B and reversal experiments at equivalent pressures in Figure 10. The compositional range is identical for SSD and MSD decompressions down to 150 MPa, even though the total groundmass crystallinity of the SSD run is significantly greater (20% versus 6%). A reversal experiment produced the same compositional range. For decompressions to 100 MPa, plagioclase grown in the SSD experiment is slightly more evolved (An_{35} typical) than that observed in the MSD run (An_{40}). The spread between the compositions and mode of feldspar produced in SSD and MSD runs increases in the 75-MPa experiments, where the average composition in SSD experiments is An_{26}, and the MSD feldspars remain near An_{40}. This spread is probably a result of the higher crystallinity and more evolved melt in the SSD experiment. At 50 MPa, where the crystallinities produced by MSD and SSD are similar, the compositions overlap, with the dominant composition in both runs An_{27-33}. The 10-MPa data are intriguing. The greater crystal content and more evolved melt in the SSD run relative to the MSD sample (ϕ = 63 and 26%, respectively) accounts for the formation of alkali feldspar in the former. However, microlites in the SSD run appear to indicate a smaller solvus region. That is, the crystals in the SSD experiment have similar Ab:An ratios, but greater Or content. This appears to reflect less efficient element partitioning in the SSD run, so that feldspar similar in composition to the melt (rather than the equilibrium composition) forms following supersaturation [*Smith and Brown*, 1988]. The partition coefficient of Ca/K between microlites and groundmass glass, $(Ca/K)_{Pl}/(Ca/K)_{glass}$, is up to ~3 times greater in the MSD experiment (310) than the SSD run (120) in these experiments. Investigation of plagioclase growth upon decompression in nature [*Nakada and Motomura*, 1999] and experiments [*Geschwind and Rutherford*, 1995] demonstrates that decreased partitioning is correlated with rapidly imposed supersaturation, and thus higher ΔT_{eff} at the onset of crystallization.

[29] Because only a few microlites were observed in the series A 5-MPa experiment, the crystals present in the 931-hour run are shown with the MSD experiment in Figure 10f. As noted earlier, the crystal contents resulting from SSD and MSD are reversed at 5 MPa from the trends at higher pressures (Figure 7e). Consequently, the feldspar compositions in the MSD runs extend to alkali feldspar (Or_{58}), while the dominant composition in the 931-hour run is plagioclase (An_{33}), with ternary feldspar ($Ab_{69}An_{11}Or_{20}$) occurring in contact with groundmass quartz.

[30] Because of their small size, microlite compositions are not available for SSD experiments less than 168 hours in duration.

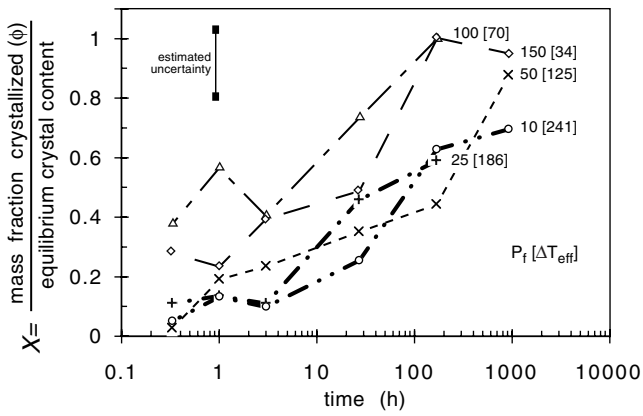

Figure 9. Fraction transformed (X) with time for several P_f. The value X is determined as the total groundmass crystallinity (Qtz + Fs) normalized by the equilibrium crystal content (curve in Figure 2). Final pressures and effective undercoolings (P_f, in MPa [ΔT_{eff} in °C]) are noted to the right of each trend.

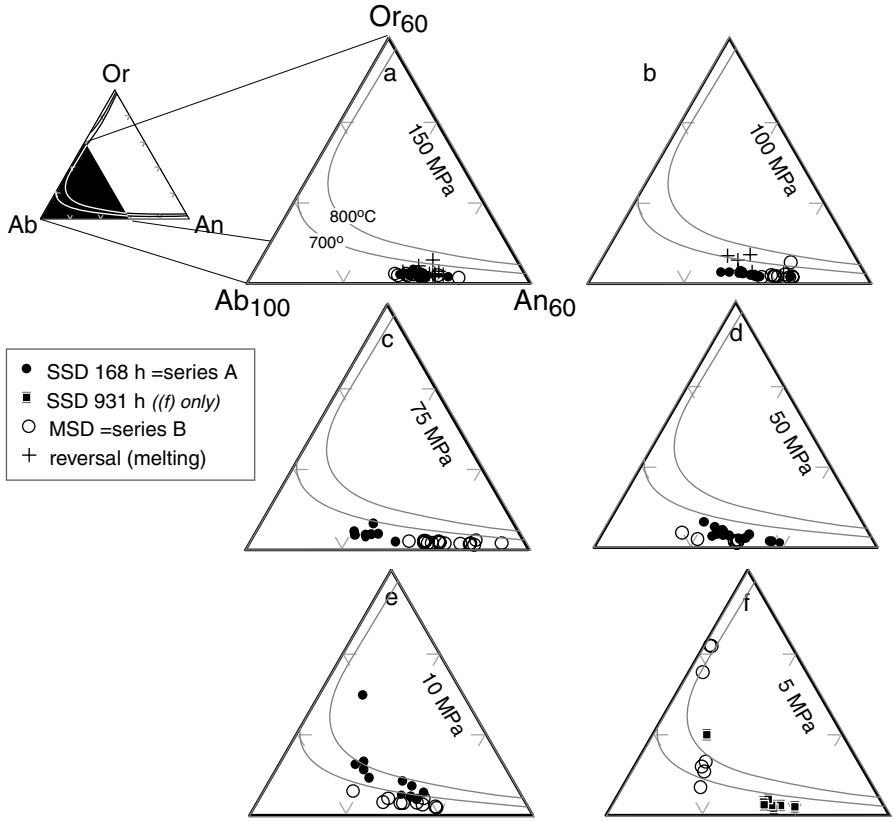

Figure 10. Feldspar microlite compositions in two time series SSD experiments, all MSD runs, and two reversal experiments. P_f is indicated in each plot. Compositions become progressively more evolved with decreasing P_f and increasing total crystal content. Below 150 MPa, SSD microlites are generally more evolved than MSD microlites, except for P_f = 5 MPa, where the relationship is reversed. Solvi for the anhydrous feldspar system at 700 and 800°C and 100 MPa [*Nekvasil*, 1992] are shown for comparison.

Microlites were not present in SSD experiments at 150 MPa for 931 hours or in 168-hour experiments at 5 MPa. Thus examination of evolving composition with time among SSD runs is limited to series A and the 931-hour experiments at 50 and 10 MPa (Figure 11). Albitic plagioclase from An_{38} to An_{20} found in the 168-hour, 50-MPa run are also observed at 931 hours, with alkali feldspar of Or_{61}, also appearing in the longer experiment. The total feldspar mode increases from 17 to 32% in this interval. Or-rich feldspar in the longer run is ubiquitous at the tips of plagioclase laths and intergrown with quartz, yet their small size made analysis very difficult. Feldspars in the 168-hour, 10-MPa experiment are ternary in composition (e.g., $Ab_{70}An_{21}Or_9$) with a small amount of alkali feldspar ($Ab_{62}An_9Or_{29}$) occurring at the tips of the plagioclase laths. After 931 hours at this pressure, alkali feldspar ranges to $Ab_{34}An_2Or_{64}$ and no longer grows solely in contact with plagioclase. Instead, alkali feldspar crystals are dendritic bladed aggregates and also occur in rimming and intergrowth relationships with quartz. The total feldspar content increases only slightly (43–48%) in this time interval.

[31] The evolution in feldspar compositions as a function of increasing total crystallinity and evolving melt is consistent with the low-pressure, H_2O-saturated phase relations in the system Q-Ab-An-Or-H_2O with a_Q = 1 [*Stewart and Roseboom*, 1962; *Nekvasil*, 1992]. Plagioclase crystallizes alone until the melt composition intersects the two-feldspar curve. If the melt intersects the curve along the ''high-temperature'' portion, cotectic crystallization of plagioclase and Or-rich alkali feldspar occurs. However, the alkali feldspar-plagioclase rimming relationship observed in the early stages of alkali feldspar crystallization suggests that the liquid intersects the two-feldspar boundary at the peritectic portion of the curve. Here plagioclase reacts with the melt to produce alkali feldspar. With continued crystallization the melt moves toward the thermal minimum, which is off the curve and in the alkali feldspar field, for the remainder of the crystallization sequence.

4.3. Feldspar Textures

4.3.1. Series A. [32] Feldspar microlite morphology and abundance vary systematically with P_f in series A samples (Figures 3 and 11). As P_f decreases, microlite morphology changes from compact euhedral to hopper, swallowtail, and finally high aspect ratio tablets. This evolution is similar to that observed in isothermal and constant rate cooling experiments with increasing ΔT [*Lofgren*, 1974; *Corrigan*, 1982; *Kouchi et al.*, 1986]. For $P_f >$ 100 MPa, microlites are relatively large, faceted, subequant, and sparse. Crystals grown at 100 MPa are more elongate, hopper-formed, and moderately abundant. Microlites grown between 75 and 50 MPa are more elongate and display skeletal as well as cellular forms (swallowtail and hopper). At 25 MPa, there is a dramatic increase in the population density of crystals, as well as in aspect ratio and alignment of crystals. Parallel laths (Figure 3d) may actually be connected in the third dimension, but crystals are too small for determination of optical continuity. At 10 MPa, crystals are smaller, densely populated in radiating clusters, and highly elongate. Increasing aspect ratio with decreasing P_f is characteristic of the series A experiments (Figure 12). The experiment at 5 MPa produced a dramatically different texture from the other runs. This sample contains a negligibly small volume of microlites and is characterized by inhomogeneous

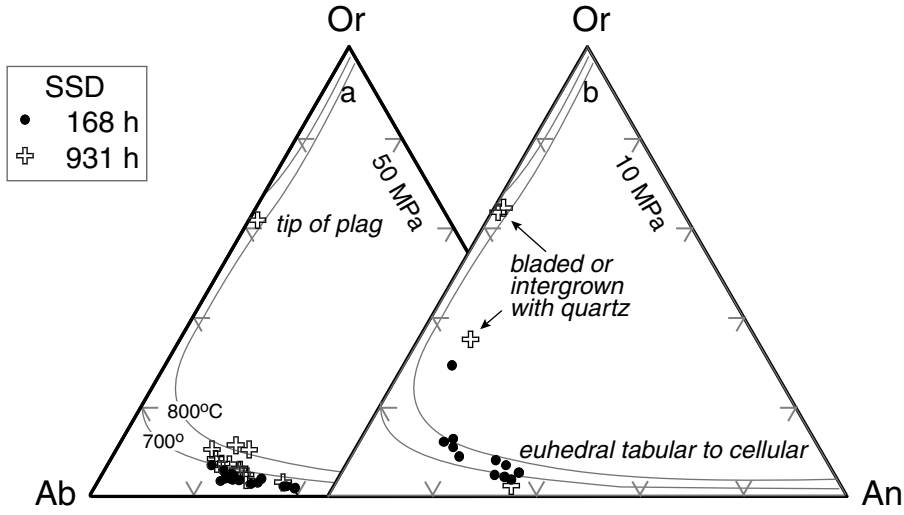

Figure 11. Feldspar microlite compositions for (a) 50 MPa and (b) 10 MPa SSD experiments held for 168 and 931 hours. Composition is related to morphology: plagioclase crystals exhibit euhedral tabular to cellular morphologies and occur primarily as individual grains, while alkali feldspar occurs as rims on plagioclase and intergrown with quartz. Solvi for the dry feldspar system at 700 and 800°C and 100 MPa [*Nekvasil*, 1992] are shown for comparison.

matrix, extensive reaction of plagioclase phenocrysts with melt, and pervasive intergrowth of quartz and alkali feldspar.

4.3.2. Series B. [33] The relationship between SSD versus MSD supersaturation conditions and crystal habit is analogous that of plagioclase crystals growing in response to isothermal and constant-rate cooling of basaltic melts [*Corrigan*, 1982]. That is, a similar range in crystal morphologies appears in series B, but the conditions at which noneuhedral forms appear are displaced to lower P_f (Figure 4). There is no distinct population of small microlites in experiments with P_f > 100 MPa. Rather, most crystals are large, subequant, and zoned, making the distinction between microlites and rimmed phenocryst fragments very difficult. Many feldspar crystals are mottled or distinctly zoned in BSE images (e.g., Figures 4a and 4b), reflecting compositional inhomogeneity. Rare clusters of elongate tablets are present, but most crystallization occurs as planar faceted growth of existing fragments. Constitutional supercooling becomes important at P_f below 100 MPa, evidenced by dendritic growth at the corners of crystals [*Porter and Easterling*, 1997]. In 50- and 25-MPa runs, zoned microlites and rimmed fragments have swallowtail terminations. In the 10-MPa experiment, hopper morphologies occur in addition to swallowtail and tabular forms. Irregular zoning patterns indicate that most crystallization is due to growth of phenocrysts and preexisting fragments. There is no way of knowing the sizes of the original fragments, so quantitative assessment of crystal growth rate in these runs is impossible.

[34] In all experiments above 5 MPa the glass between crystals is homogeneous and optically clear. There is no evidence of quartz crystallization in the groundmass, although growth of phenocrysts must have occurred according to mass balance calculations (Figure 7d). Textures in the 5-MPa experiment starkly contrast the other runs. This is the only MSD experiment in which microlite nucleation significantly increased the overall crystallinity. Groundmass crystallization of anhedral feldspar and interstitial quartz is pervasive (as in top corners of Figure 4f). Small tabular plagioclase microlites have moderate aspect ratios (L/W typically 3–7) and alkali feldspar tips. The number density of these microlites outside the regions of micron-scale quartz-feldspar intergrowth is ~40,000 mm^{-2}. Thus the area concentration of microlites in this experiment surpasses that of all the series A experiments.

4.3.3. Temporal evolution. [35] Feldspar microlite growth rate, morphology, aspect ratio, and size reflect the degree and timing of imposed supersaturation and the duration of the crystallization interval. Crystal form varies with both run time and P_f. Each series of experiments at 150, 100, 50, 25, and 10 MPa produced a characteristic size and morphologic evolution in time, summarized graphically in Figure 12.

[36] Crystals in the 150-MPa series are euhedral, with planar faceted habits. Length to width ratios (L/W) are typically <5 for all runs, but the size of the largest microlites first increases, then decreases with time after 27 hours (Figure 12b). Interestingly, euhedral microlites were not observed in either of two experiments run at 150 MPa for 931 hours. Instead, large feldspar crystals and fragments are rimmed with new growth, much like the MSD experiment textures (e.g., Figure 4b).

[37] Microlites in the 100-MPa series are acicular needles (L/W = 10–15) at short times, developing into increasingly compact, hopper forms with planar exterior faces after 27 hours. By 168 hours, the average L/W ratio is <5 (Figure 12a). Microlite size continues to increase in proportion to the logarithm of time.

[38] A shift in the morphological evolution of crystals over the experimental timescales occurs between P_f = 100 and 25 MPa. At 50 MPa, crystals in the shortest runs are faceted, euhedral, and highly variable in aspect ratio (L/W = 1–15). Between 3 and 168 hours, crystals evolve from highly elongate to swallowtail to hopper-formed. Crystal size increases steadily with the log of time until 27 hours, then triples between 27 and 168 hours (Figure 12b). Size and aspect ratio after 168 hours could not be accurately measured due to the high degree of crystal interpenetration in the 931-hour run (Figure 5b).

[39] Likewise, microlites at 25 MPa start out equant, evolve to a thready, nonfaceted morphology by 27 hours, becoming highly elongate skeletal forms by 168 hours. The parallel and radiating orientation of laths in Figure 3d may represent a two-dimensional slice through the blades of a single radiator-shaped three-dimensional (3-D) structure or axiolitic spherulite. Because the sizes of the potential aggregates could not be verified, these features were treated as individual crystals for the nucleation and growth rate, size, and L/W measurements. (If these parallel laths are not individual crystals, it is estimated that the nucleation rate could be overvalued by a maximum of one order of magnitude.)

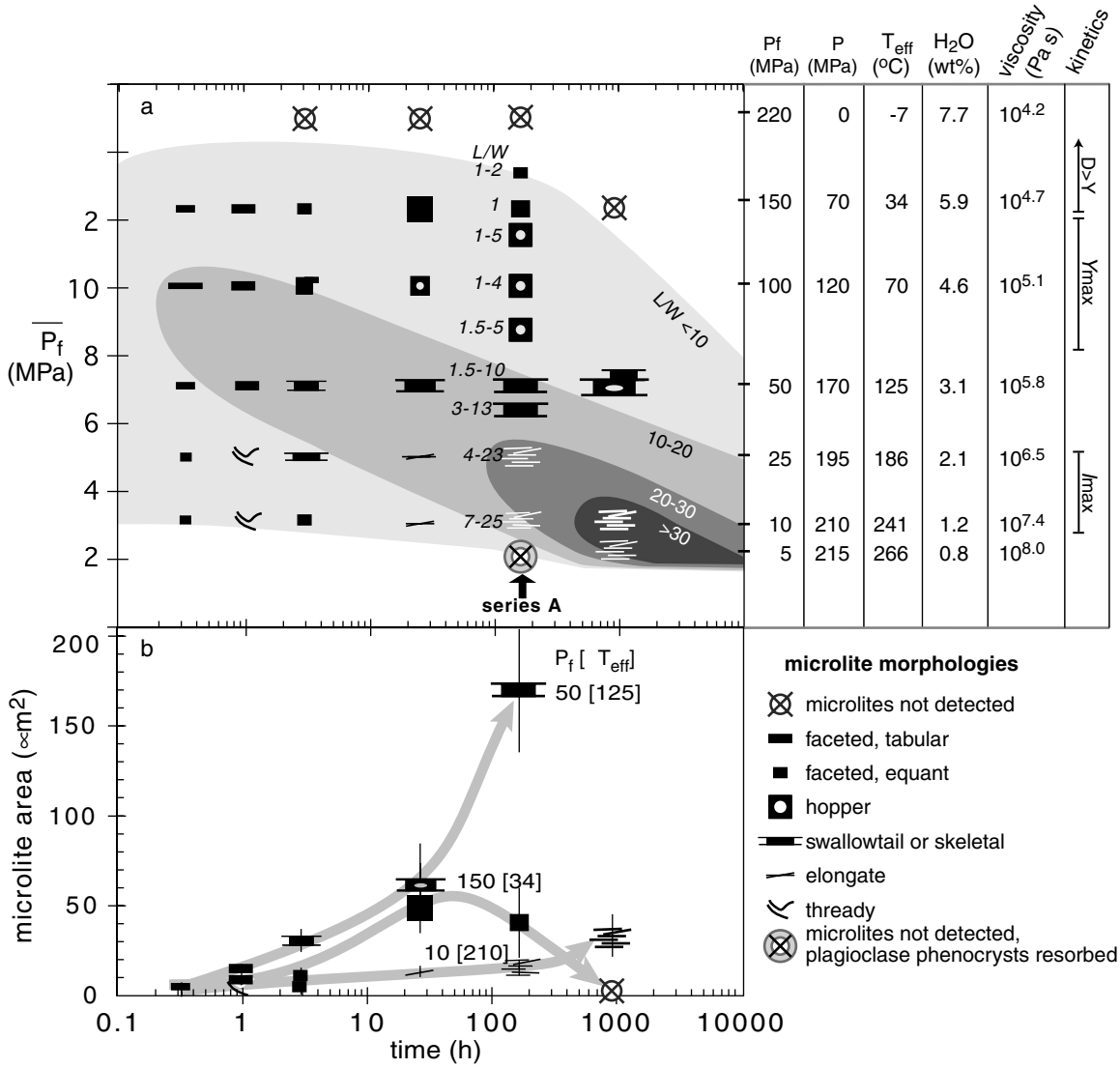

Figure 12. (a) Graphical representation of feldspar microlite habit, aspect ratio (L/W), and relative size for all SSD experiments. Tabulation at right includes dissolved melt H_2O content following decompression and prior to crystallization calculated using the P33 matrix glass composition and an empirical solubility model [*Moore et al.*, 1995]. Viscosity is calculated [*Hess and Dingwell*, 1996] for P33 melt at the saturation H_2O contents and experimental pressure and temperature. Conditions where diffusion of feldspar components in melt appears to be rapid compared to crystal growth are indicated by arrow marked "$D > Y$." Conditions of maximum crystal growth rate (Y) and nucleation rate (I) are indicated at right. (b) Microlite size and morphology through time for three time series. P_f = 150 MPa: The decrease in microlite size between 27 and 168 hours and subsequent disappearance of microlites by 931 hours indicate textural maturation of the crystal population. Neither the composition of the matrix glass nor the mode of crystallizing phases changed between 168 and 931 hours, suggesting that chemical equilibrium was attained in less than a week. In this case, feldspar components are apparently redistributed from microlites to phenocrysts, resulting in overall grain coarsening. $P_f \leq 50$ MPa: Aspect ratio increases with time, and samples do not attain chemical equilibrium in experiment timescales. One interpretation is that the patterns of textural evolution at different ΔT_{eff} conditions represent different stages in a general sequence of morphological change. In cases where melt viscosity is relatively low (such as at high P_f), and at the early growth stages of low P_f experiments, long-range diffusion of components toward the nucleus is not important. For $P_f < 150$ MPa a boundary layer of melt depleted in feldspar-forming components and enriched in rejected components develops around the crystal due to insufficient rates of mass transport to/from the interface. Protuberances grow faster than planar surfaces because of this constitutional supercooling [*Dowty*, 1980]. Series at low P_f/large ΔT_{eff} show only the early portion of this process, with aspect ratio increasing over time (Figures 5c and 12a). Presumably, the highly anhedral morphologies observed at these conditions would eventually coarsen into euhedral faceted grains given much longer run durations.

[40] The 10-MPa series undergoes a similar morphological trend from equant euhedral forms at short times, evolving to highly elongate acicular habit between 27 and 168 hours. The average size of crystals slowly increases with log time up to 168 hours, then doubles by 931 hours (Figure 12b). By 931 hours the groundmass is 70% crystallized, filled with bladed and fan-shaped plumose spherulitic, interpenetrating feldspar crystals (Figure 5d). Microlite aspect ratio is highly variable and generally increases with time.

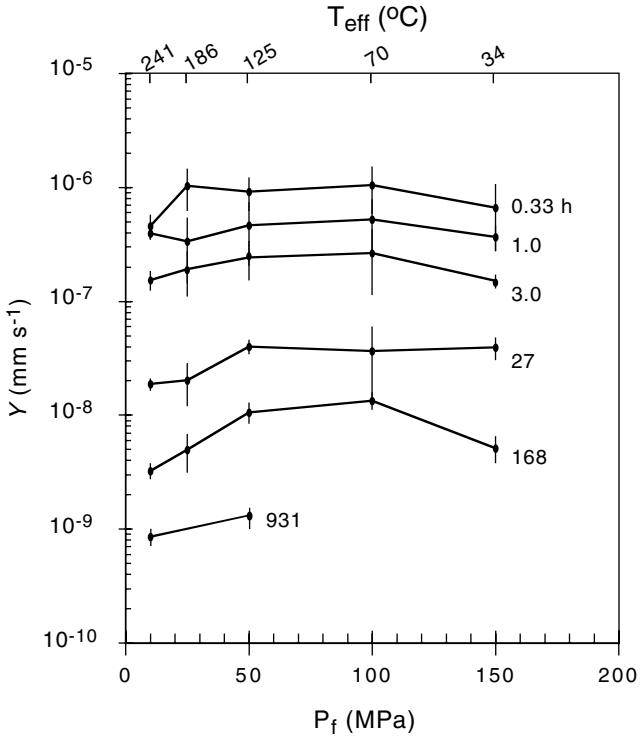

Figure 13. Microlite growth rate isochrons for SSD experiments.

The matrix glass between crystals is inhomogeneous (Table 3) and finely vesicular in the most crystalline regions.

[41] Growth rates in SSD experiments decrease by 3 orders of magnitude between 0.33 and 931 hours following decompression (Figure 13). Initial crystal growth rates (t = 0.33 hour) appear to be independent of pressure, although this may be a result of uncertainty in measurements at very low crystal fractions. Beginning at 3 hours the curves develop a maximum at 50–100 MPa. This feature is examined further in Section 4.4 using data from series A samples. Within the 1σ error associated with average values of maximum growth rate, each series of runs at a given P_f obeys a $Y = \alpha t^{-0.5}$ relationship consistent with crystal growth limited by the rate of diffusion of components in the melt to or away from the crystal interface [*Kirkpatrick*, 1981]. Assuming that $Y = 0$ at $t = 0$, the proportionality constants, α, range from 2.9×10^{-8} (10 MPa series) to 5.6×10^{-8} (100 MPa series) and average 4.4×10^{-8} ($1\sigma = 1.1 \times 10^{-8}$). Within the error associated with the measurements, there is no significant relationship between P_f (and thus melt H_2O content and viscosity) and α, as expected for a diffusion-limited process.

[42] An alternative explanation for decreasing y with time is a progressive decrease in undercooling during experiments. According to classical theory the rate of crystal growth is related to the total free energy change of the system upon crystallization, which increases with ΔT [*Dowty*, 1980]. Systems approaching equilibrium are thus expected to crystallize ever more slowly, until $Y = 0$ at $\Delta T_{eff} = 0$. Unlike traditional crystallization experiments [e.g., *Klein and Uhlmann*, 1974; *Kirkpatrick*, 1981] where the growth mechanism is determined from short-duration (effectively constant ΔT) experiments, the changes in melt composition and thus driving force for crystallization following decompression in the present experiments are significant. Melts start out undercooled (ΔT_{eff} = 19–266°C) and many approach chemical equilibrium ($\Delta T_{eff} = 0$) less than 168 hours after decompression. Even runs at P_f < 100 MPa (largest initial ΔT_{eff}) are at least halfway to equilibrium crystallinity by this time.

4.4. Nucleation and Growth Kinetics

[43] The SSD experiments provide the most straightforward approach to obtaining nucleation and growth rates at a given value of ΔT_{eff} produced by decompression. Ideally, nucleation rates are determined from the shortest-duration SSD decompression experiments, as they record the initial response of the system to undercooling at the largest possible supersaturation for a given P_f. However, the scarcity of crystals in runs <27 hours in duration, combined with the ambiguity in distinguishing small phenocryst fragments from internally nucleated microlites, resulted in large uncertainties in the growth and nucleation rate calculations. In several of the longest runs, interpenetrating groundmass crystallization was so pervasive that individual crystals could not be discerned; kinetic measurements under these conditions are also impossible. Therefore we use series A textures (summarized in Figure 14) to examine the kinetics of nucleation as a function of imposed supersaturation. The nucleation rates obtained are time-integrated values significantly lower than the initial rates. However, the functional dependencies of the rates on ΔT_{eff} should scale together, so that the measured curves are useful as indicators of relative nucleation rate at different undercoolings.

[44] Crystal number densities varied dramatically in the 168-hour runs, ranging from 20 to 12,000 mm^{-2} with a maximum at 10–25 MPa (Figure 14). Calculated nucleation rates likewise varied by nearly 3 orders of magnitude (Figure 15a). Crystal nucleation, I, and growth rates, Y, follow the classical bell-shaped curves with ΔT_{eff} observed in cooling experiments and predicted by theory [*Tammann and Mehl*, 1925; *Jackson*, 1969]. At low supersaturations (high P_f), nucleation and growth are low because the thermodynamic driving force (free energy difference between liquid and solid phases) for crystallization is small. With increasing ΔT_{eff}, this driving force becomes substantial and the rates of nucleation and growth increase. Eventually, increasing melt viscosity (due to devolatilization) reduces the mobility of feldspar-forming components in the melt and inhibits these processes. (Viscosity of the reference melt with degassing is shown in Figure 1c.) Thus, although supersaturation continues to increase with ΔP, growth and nucleation become increasingly suppressed as the melt degasses. The observed P_f-Y relationship (Figure 15b) has a broad peak centered at moderate P_f (100 MPa, ΔT_{eff} = 70°C), and the maximum I occurs at lower P_f (10–25 MPa, ΔT_{eff} = 186–241°C). Rates of both nucleation and growth are extremely low at the lowest P_f (5 MPa, ΔT_{eff} = 266°C).

5. Discussion

[45] Several key results from the compositional and textural analysis of the products of variable-duration, variable-rate decompression experiments form the basis of further analysis and application to natural systems. These include the following: (1) Crystal nucleation and growth rates are bell-shaped functions of ΔP (or ΔT_{eff}), consistent with classical theories and previous studies of cooling-driven crystallization. (2) Chemical equilibrium is achieved in <1 week for samples rapidly decompressed by moderate amounts; samples decompressed to <40 MPa do not achieve equilibrium because of insufficient plagioclase feldspar crystallization. (3) Following rapid decompression to different final pressures, the liquid lines of descent do not proceed directly toward the granite minimum composition. (4) For a given rapid decompression rate, melts decompressed a small amount respond by crystallizing sooner than those decompressed a large amount. Regardless of P_f, the approach to equilibrium crystallinity is proportional to the log of time. (5) The liquid line of descent and fractional approach to equilibrium for melts brought to a given final pressure differs according to decompression rate. (6) With increasing ΔP (and similar IDR), feldspar compositions in SSD samples are in turn equal to, more evolved than, then less evolved than the corresponding MSD samples. (7) The morphologic

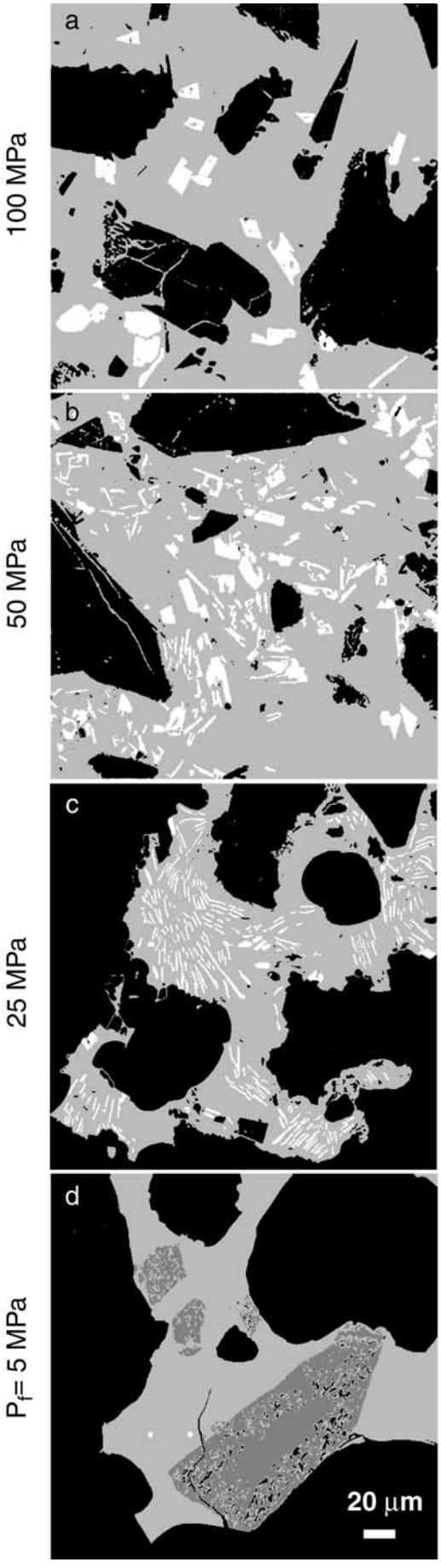

evolution of crystals with increasing ΔP and time is similar to previous experimental results from cooling experiments. There are stark contrasts between SSD and MSD samples for a given P_f, indicating that decompression path is critical in controlling texture. (8) Nucleation and growth rates decay over time. This may be due to either to lessening thermodynamic driving force for crystallization or long-range diffusion control of these processes. Many of these observations can be interpreted in view of the relative rates of nucleation and growth as a function of ΔT_{eff} associated with different decompression paths.

5.1. Textures and Chemical Equilibrium: Relation to Nucleation and Growth Kinetics

[46] The relative rates of feldspar nucleation and growth exert a profound influence on the textures, compositions, and mode in the SSD runs. Four crystallization regimes defined by relative rates of nucleation and growth are summarized in Table 4. The relationships suggest that each of the textural and compositional characteristics in the SSD experiments is directly dependent upon the relative magnitudes of I and Y at the given P_f (Figure 15). Since these processes have maxima at different ΔT_{eff}, their controls on crystal characteristics can be compared. Two obvious examples are the correlation between I and crystal number density (both large at $\Delta T_{\text{eff}} = 186°C$), and between crystal size and growth rate (peaking at $\Delta T_{\text{eff}} = 70°C$). Morphologies are diagnostic indicators of ΔT_{eff}, displaying a very similar sequence to that described by *Lofgren* [1974]. Equant, faceted tabular crystals reflect slow growth relative to component diffusivities at small ΔT_{eff} (34°C), while cellular crystal morphology demonstrates the reverse relationship at larger ΔT_{eff} (70°C; Figure 12). Increasing ΔT_{eff} further (to 125–186°C) enhances the disparity between growth rates and diffusion rates, resulting in acicular and spherulitic morphologies. Faster nucleation at high undercoolings boosts crystal number density, contributing to an overall decrease in crystal size. However, with even greater ΔT_{eff} (266°C), the kinetics of plagioclase microlite nucleation become too slow for a significant (discernable) number of crystals to form in 168 hours.

[47] Progress toward chemical equilibrium at a given time is a combination of the kinetics of nucleation and growth of all saturated phases. In SSD experiments, equilibrium is achieved at small to moderate ΔT_{eff} chiefly by growth of existing plagioclase and quartz crystals and sparse nuclei. At large ΔT_{eff} (70–250°C), where growth rates slow and nucleation rate increases, microlite formation becomes the dominant crystallization process, as demonstrated by high number densities of extremely small, elongate crystals (Figures 3 and 14). In the interval between maximum I and Y, chemical equilibrium is not achieved during the 168-hour runs, and the delayed crystallization response at P_f = 50 MPa may simply result from the sluggish kinetics of both nucleation and growth of feldspar. Departure from chemical equilibrium at these pressures is a result of the steep increase in equilibrium crystal content near 50 MPa and the coincident kinetic constraint that both crystallization processes are relatively slow (Figure 15). Finally, at very high ΔT_{eff}, again where both nucleation and growth are slow, crystallization occurs by reaction of plagioclase phenocrysts with melt and alkali feldspar-quartz intergrowth rather than microlite nucleation. Inconsistent proportions of crystallizing quartz and

Figure 14. (opposite) Maps constructed from BSE images showing changes in microlite size, morphology, and spatial distribution with P_f for series A experiments. In Figures 14a–14c, white, feldspar microlites; gray, glass; black, vesicles and phenocryst areas that are excluded from the microlite number density calculation. In Figure 14d, gray values are as in Figures 14a–14c except plagioclase phenocrysts (dark gray) are differentiated from vesicles to show resorption texture. Scale bar in Figure 14d applies to all images.

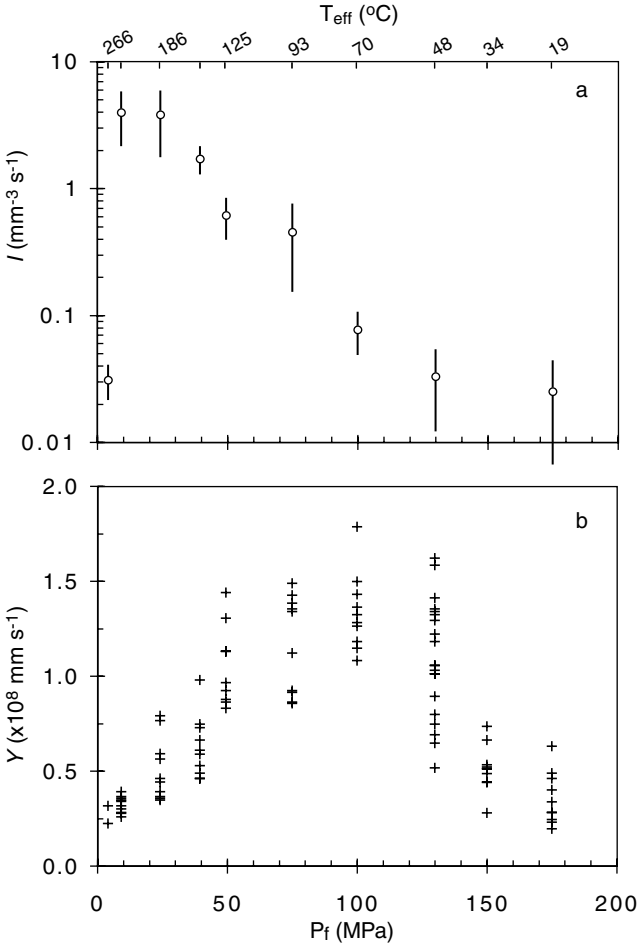

Figure 15. (a) Nucleation rate (I) and (b) growth rate (Y) data for series A experiments. In Figure 15a, error bars represent 1σ among multiple BSE images processed from each sample. Experiments at 150 MPa are not shown because late stage pressure fluctuations affected nuclei density. In Figure 15b, growth rates are calculated for the 10 largest microlites in each sample. Single values referenced in text and figures are averages of these data.

feldspar that were evident in the long-duration experiments may indicate that nucleation of one or both of these phases is sensitive to perturbations in the concentration of the other.

[48] Interpreting the MSD experiments is more difficult because effective undercooling at any point in the experiment depends on the crystallization efficiency in all the previous steps. In contrast to the SSD runs the MSD experiments do not achieve equilibrium crystal contents at any final pressure and are subsidiary to SSD crystal contents for all conditions except P_f = 5 MPa (Figure 7e). It may seem counterintuitive that the slowly decompressed samples were less likely to achieve chemical equilibrium than their rapidly decompressed counterparts over most P_f conditions (P_f > 5 MPa). However, this result and the reverse trend at P_f = 5 MPa are both consistent with the relative rates of crystallization processes experienced throughout each type of decompression. One important difference between decompression styles is that lower effective undercooling was imposed on the MSD melts. That is, for any given P_f, stepwise decompression produced smaller ΔT_{eff} throughout the run than in the SSD experiments because (1) each decompression step was 1/10 of the total ΔP and (2) crystallization during each decompression step brings the system closer to equilibrium and thus further lowers the degree of effective undercooling. For P_f falling between the growth and nucleation peaks or at pressures below the nucleation peak (Figure 15), MSD experiments come closer to achieving or surpassing the degree of crystallization produced by SSD (Figure 7e) because the slowly decompressed samples pass through conditions where these processes are rapid. Again, the difference is most pronounced in the P_f = 5 MPa runs, in which MSD results in ~20% greater total crystallinity than the SSD run. The rapidly decompressed melt was subjected to conditions of slow nucleation and growth throughout the run, while the slowly decompressed melt crystallized under a range of kinetic conditions (including high nucleation rate) before the final decompression step to 5 MPa. Textural evidence suggests that the higher crystallinity in the MSD run is a direct result of more rapid feldspar nucleation rate in this experiment. The 5-MPa experiments reinforce the idea that nucleation rate can control progress toward chemical equilibrium and also show that simply knowing the initial pressure and rate of decompression is insufficient for predicting crystal texture or extent of crystallization. Rather, the value of P_f determines melt viscosity and consequently whether or not nucleation can proceed. In this case, melt viscosity of 10^8 Pa s prohibits nucleation in the 5 MPa SSD experiment despite large ΔT_{eff}. In contrast, the viscosity of slowly decompressed melts increased gradually, and between 10 and 5 MPa apparently struck a balance between ΔT_{eff} and viscosity that greatly enhanced feldspar nucleation.

5.2. Assessing Decompression History From Groundmass Textures

[49] Many features of natural magmas were reproduced in the experimental decompressions. The experimental data (summarized in Table 4) suggest a simple decision-tree-style approach toward determining shallow crystallization conditions from the groundmass textures of natural volcanic rocks, beginning with the most

Table 4. Summary of Observations in Series A and B Experiments[a]

P_f, MPa	ΔT_{eff}, °C	Relative Rates of Nucleation (I) and Growth (Y) at P_f	Feldspar Microlite Habit, Relative Size		Area Concentration of Microlites, mm^{-2}		Feldspar Microlite Compositional Range[b]		Relative Total Groundmass Feldspar Content ϕ
			SSD	MSD	SSD	MSD	SSD	MSD	
100	70	small I, large Y	equant euhedral, large	zoned phenocrysts[b]	small [500]	small [300]	unzoned pl	normally zoned pl	$\phi_{SSD} \geq \phi_{MSD}$
50	125	small I, small Y	swallowtail and hopper, small	zoned phenocrysts[b]	moderate [2,000]	small [400]	unzoned pl	normally zoned pl	$\phi_{SSD} = \phi_{MSD}$
25	186	large I, small Y	skeletal and dendritic, small	tabular and swallowtail	large [12,000]	moderate [1,000]	pl + afs	normally zoned pl	$\phi_{SSD} \gg \phi_{MSD}$
5	266	very small I, very small Y	resorbed phenocrysts[b]	tabular	very small [<50]	very large [40,000]	—	pl + afs	$\phi_{SSD} < \phi_{MSD}$

[a] Series A, single-step decompression followed by anneal period (SSD). Series B, multistep decompression (MSD).
[b] pl, plagioclase; afs, alkali feldspar.

variable textural characteristic, microlite number density, and drawing upon other diagnostic qualities to estimate decompression rate and crystallization pressure as follows:

[50] A sparse population of feldspar microlites (e.g., $N_A \leq 2000$ mm^{-2}) suggests modest ΔT_{eff}, and thus degassing and crystallization pressure (P) > 50 MPa. (Rapid decompression to very low pressure for a short time, the exception to this general rule, can be identified by plagioclase phenocryst resorption and intergrown quartz and feldspar.) From here, microlite abundance increases with increasing decompression rate, but crystal morphology and composition are better indicators of dP/dt. Planar faceted crystals with prominent normal compositional zonation suggest slow decompression. In this case, the melt composition (projected on the haplogranite ternary as in Figure 8a) accurately records the crystallization pressure. In contrast, cellular, dendritic, and swallowtail crystals lacking strong compositional zoning point toward rapid decompression. In this instance, fairly precise measures of crystallization pressure and duration can be found from microlite aspect ratio and morphology using Figure 12.

[51] A high abundance of microlites (N_A >1500 mm^{-2}, up to 10^5 mm^{-2}) indicates crystallization at pressures ≤50 MPa, yet at the low end of this range, microlite number density does not reliably correlate with decompression rate. For example, fast decompression to ~50 MPa produces similar microlite number densities as slow decompression to ~25 MPa, and the number of microlites formed by slow decompression to 5 MPa greatly exceeds that resulting from fast decompression to the same pressure. Instead, melt composition can be used to distinguish between end-member decompression rate possibilities. Slow decompression produces equilibrium proportions (if not modes) of feldspar and quartz, so that melts (again, projected onto the haplogranite ternary) record crystallization pressures near the appropriate cotectics. Rapid decompression produces greater overall crystallinity, but melts tend to suffer insufficient feldspar crystallization over timescales ≤1 week. As a result, the melt records unrealistically high closure pressure, which is a function of both pressure and time. Having thus determined qualitatively whether decompression was rapid or gradual, high microlite abundance constrains the crystallization pressure: high N_A with fast decompression indicates P < 10 MPa, whereas high N_A produced by slow decompression suggests $10 \leq P < 25$.

5.3. Quartz Crystallization Kinetics

[52] Quartz did not occur as isolated groundmass crystals under any undercooling conditions. Instead, crystallization occurred primarily as growth of existing crystals, in contact with plagioclase, and as a cotectic intergrowth with alkali feldspar (Figures 3a, 3f, 4f, 5b, and 5d). Eutectic intergrowths of feldspar and quartz are facilitated by the development of boundary layer concentrations of SiO_2 around growing feldspar crystals and the low entropy of fusion of quartz, which reduces the tendency for facets to form [*Petersen and Lofgren*, 1986]. If quartz crystallization is inhibited, the melt may become supersaturated with SiO_2 (as in the 931-hour 50-MPa experiment, Figure 8c), and the crystal mode may become quartz deficient (in addition to being feldspar deficient; Figures 7 and 8). Previous cooling-induced crystallization experiments show the quartz growth maximum occurring at larger ΔT than for feldspar [*Swanson and Fenn*, 1986], and the time series SSD experiments suggest that the relationship is similar for ΔT_{eff} imposed by degassing (Figure 8c).

5.4. Phase Transformation Kinetics

[53] Transformation diagrams, or time-temperature-transformation (TTT) plots, are employed in metallurgy and materials science to show the effect of undercooling on overall transformation kinetics [*Putnis*, 1992; *Porter and Easterling*, 1997]. A transformation diagram for the experimental matrix melt was determined from the SSD results as a function of P_f and ΔT_{eff} in order to further investigate the conditions of greatest bulk (quartz + feldspar) crystallization rate. Accurate TTT-style plots require data for crystallization at the incipient and near-equilibrium stages as well as intermediate intervals. Usually, the time elapsed at benchmark crystal contents, such as 5, 50, and 95%, determined from a t-X plot (such as Figure 9) are used to construct C-shaped transformation contours on a plot of t versus T. The run times required to produce very small and very large values of x were not obtained in the present set of experiments. Therefore inferences about the initial and final stages of crystallization require fitting the existing t-X data with reasonable functions and extrapolating crystal contents forward and backward in time. Linear functions and the Johnson-Mehl-Avrami (JMA) equation [*Avrami*, 1939; *Johnson and Mehl*, 1939; *Avrami*, 1940] were fit to the t-X data (Figure 16) in order to create the 5 and 95% crystallization contours on the TTT-style diagram (Figure 17). The JMA equation has been tested extensively in the study of metals, ceramic materials, and geologic systems [*Kirkpatrick et al.*, 1976; *Marsh*, 1981; *Zanotto and Leite*, 1996]. Full derivations of the equation is given by *Christian* [1965] and summarized by *Kirkpatrick* [1981].

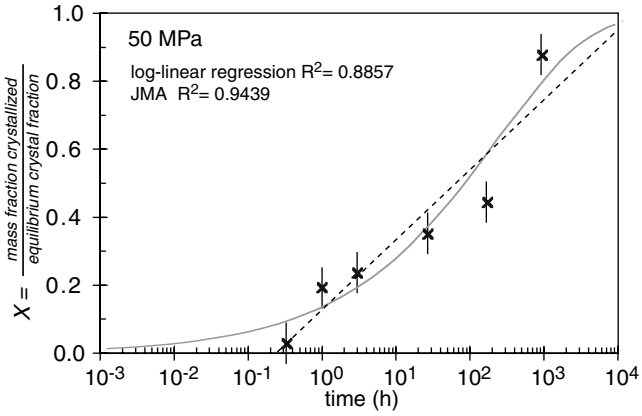

Figure 16. Plot shows log linear and JMA fits to 50 MPa t-X data from time series SSD experiments (e.g., Figure 9). The JMA equation in its most general form is $X = 1 - \exp(-Kt^n)$, where K includes a geometric factor for the morphology of the transformed phase as well as a combination of the rates of nucleation and growth and n is an integer. The form of the equation predicts that X increases sigmoidally in time. Overall transformation can be divided into three stages: an initial interval of slow crystallization as nuclei are formed and begin to grow, a period of rapid transformation in which growth occurs at many sites, and a final stage near completion in which the volume of melt remaining is small and the rate of transformation likewise decreases. For a constant value of K, decreasing n corresponds to a longer initial phase and slower overall transformation.

[54] A TTT-style diagram is created by connecting the $X = 0.05$, $X = 0.50$, and $X = 0.95$ values for the JMA and linear regressions of the t-X data (Figure 17). In this case, P_f or ΔT_{eff} take the place of temperature as the driving force for the transformation. The distribution of data and associated uncertainties are such that the JMA and linear fits of t-X data produce qualitatively similar results in the transformation diagram. The curves have two distinct minima, at P_f =100 and 25 MPa, indicating more rapid overall transformation at these conditions. These undercoolings correspond to the conditions of maximum feldspar growth and nucleation rate independently determined from textural data (Figure 15).

[55] This result is important for modeling crystallization of degassing systems. Either feldspar nucleation or growth may dominate transformation kinetics, so that in certain circumstances one or the other contributes negligibly. At other conditions, both processes must be considered. The dual minima are interpreted to

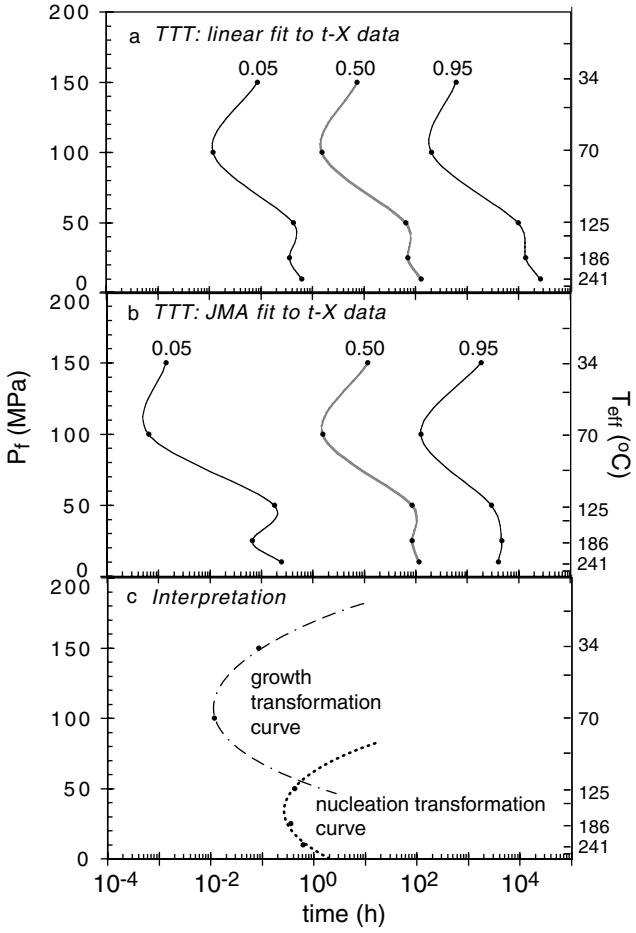

Figure 17. TTT-style diagrams based on *t-X* data (e.g., Figure 9) and regressions for series A experiments (Figure 16). Contours represent 0.05, 0.50, and 0.95 mass fraction crystallized. (a) Equidistant transformation curves, arising from log linear fits to *t-X* data. (b) The JMA-derived curves primarily differing in the small (0.05) and large (0.95) values of x due to the sigmoidal shape of the inferred transformation history (Figure 16). The deep "knee" at 100 MPa is due to the significant crystallization at short times (Figure 9). (c) Double minima thought to reflect two crystallization regimes, one dominated by crystal growth and the other by microlite nucleation.

correspond to the superposition of two C-shaped curves corresponding to the nucleation of new crystals and the growth of existing and newly formed crystals (Figure 17c). The minimum time for incipient ($X = 0.05$) crystallization by nucleation is greater than the minimum time for incipient growth-dominated crystallization. This seems to contradict the normal sequence of nuclei formation followed by growth but simply indicates that growth of existing crystals begins after a shorter time period than the generation of new nuclei, even under the most favorable nucleation conditions. The TTT plot demonstrates the utility of using a natural crystal-bearing starting material for the experiments. Magmas entering shallow volcanic conduits usually contain crystals; Figure 17 shows the conditions where their presence is important and to what extent their growth dominates the crystallization process.

5.5. ΔT_{eff}, Groundmass Texture, and Eruption Style

[56] Small ΔT_{eff}, generated by either small ΔP and fast decompression or moderate ΔP and slow decompression, produces large, faceted, compositionally zoned crystals because growth rate is fast relative to nucleation rate and diffusion of feldspar components in the melt is not rate limiting. Not surprisingly, this crystal texture is commonly observed in exterior (quenched) samples of dome lavas such as those of Mount St. Helens, Washington [*Cashman*, 1988], Soufriere Hills, Montserrat [*Cashman and Blundy*, 2000], and Merapi, Indonesia [*Hammer et al.*, 2000].

[57] Either fast decompression to moderate pressure or slow decompression to low pressure will impose greater ΔT_{eff}. In these cases, diffusion of crystal components in the melt becomes important, resulting in more numerous microlites and skeletal morphologies. In natural silicic magmas, abundant microlites of tabular and swallowtail morphologies are associated with moderately explosive eruptive styles and intermediate mass discharge rates [*Klug and Cashman*, 1994; *Wolf and Eichelberger*, 1997; *Gardner et al.*, 1998; *Hammer et al.*, 1999].

[58] Pervasive phenocryst-melt reaction and delayed feldspar microlite formation were observed only in the greatest imposed ΔT_{eff} condition: rapid decompression to very low P_f for a moderately short time. Presumably, this transient texture develops during a feldspar nucleation induction period, since a longer experiment at this pressure produced abundant microlites and significant groundmass crystallization. This and other samples held at low pressure for long durations (sustained large ΔT_{eff}) developed inhomogeneous matrix material and extensive intergrowth of crystal phases. In nature, patchy distribution of Na_2O-rich melt and K_2O-rich melt with acicular feldspar nucleating at the boundary is associated with near-surface magma residence at relatively high temperatures (e.g., Mount St. Helens 1980 blast dacite and interior samples of the 1980–1986 domes [*Cashman*, 1992]) and has been interpreted as incipient devitrification. Alternatively, this inhomogeneous matrix may arise from local fractionation of plagioclase and alkali feldspar. For example, high K_2O concentration would result from insufficient alkali feldspar crystallization in the melt around rapidly growing plagioclase. Similarly, rapid coprecipitation of alkali feldspar and quartz enriches the CaO and lowers the SiO_2 contents of the surrounding melt. Subsequent crystallization of these highly undercooled melts could result in fine crystalline intergrowths. Although slow cooling may contribute to the postextrusion development of patchy groundmass glass observed in dome interiors, these experiments demonstrate that the texture may also develop isothermally.

6. Conclusions

[59] This study demonstrates and quantifies several of the links between decompression history and the textures and compositions of crystals grown as a result of melt degassing. The number, composition, and morphology of feldspar microlites growing from an undercooled melt depend on the balance between the thermodynamic driving force (ΔT_{eff}) and kinetic barriers (particularly arising from melt viscosity) resisting nucleation and crystal growth. Because the solubility of H_2O in rhyolite melt is a nonlinear function of pressure, both melt viscosity and ΔT_{eff} increase steeply below 50 MPa. ΔT_{eff} can also decrease over time at a given P_f because melts crystallize and approach chemical equilibrium. Thus the value of P_f, magnitude of ΔP, and decompression rate, all control ΔT_{eff} and melt rheology and ultimately the kinetics of feldspar nucleation and growth. Depending on undercooling conditions, either nucleation or crystal growth can control the rate of bulk phase transformation from liquid to solid. Rapid crystal growth at low to moderate ΔT_{eff} allows the fastest overall transformation and thus the quickest route to chemical equilibrium, despite modest thermodynamic driving force. High rates of crystal nucleation at large ΔT_{eff} define the second-most efficient crystallization regime, but very high ΔT_{eff} constitutes a poor condition for rapid transformation. Feldspar nucleation is optimal over a narrow interval, requiring a large free energy difference driving crystal-

lization, but is inhibited by the rapid increase in melt viscosity with decreasing pressure.

[60] A primary motivation for this study was to test the idea that a detailed history of syneruptive magma degassing of silicic magmas is recorded in the groundmass textures of erupted materials. The chosen starting composition, effectively the rhyolite groundmass glass of natural Pinatubo dacite, is similar to the matrix glasses of many natural dacites and andesites. The results described herein should be broadly applicable to a wide range of calc-alkaline magmatic systems, as the matrix melt compositions tend to be near the granite minimum [e.g., *Hildreth*, 1983; *Gardner et al.*, 1995; *Barclay et al.*, 1998; *Hammer et al.*, 1998; *Nakada and Motomura*, 1999] and saturated with feldspar at the onset of ascent.

[61] Eruption parameters of interest include decompression rate, depth where degassing occurs, and residence time at shallow levels (if magma pauses en route to the surface). Narrow ranges of these parameters are mimicked using different duration MSD and SSD experiments to varying final pressures. Important restrictions to the application of these results to natural volcanic products arise from simplifying assumptions and experimental limitations. (1) Crystallization intervals shorter than 27 hours cannot be resolved because textures are not well developed, and intervals longer than 6 weeks (for fast decompression) or 2 weeks (for slow decompression) are beyond the scope of the study. (2) Lower decompression rates, longer-duration linear decompressions, accelerating decompression rates, and multiplateau depressurizations are all feasible *P-t* paths experienced by magmas that were not investigated. (3) Experiments were purely isothermal. In nature, magma temperature may decrease during degassing as H_2O exsolution consumes the heat of vaporization and/ or by adiabatic expansion of vapor bubbles during decompression. Other processes, such as release of latent heat of crystallization [*Sahagian and Proussevitch*, 1996; *Toramaru*, 2001] and viscous dissipation during flow [*Polacci et al.*, 2001], will also tend to change the temperature of the magma.

[62] **Acknowledgments.** Joe Devine, Mike Jercinovik, and Michael Shaffer assisted with electron microprobe analysis and SEM imaging at Brown University, University of Massachusetts at Amherst, and the University of Oregon, respectively. We thank Paul Hess, Yan Liang, and Kathy Cashman for fruitful discussions. The comments and suggestions of Jon Blundy and an anonymous referee are greatly appreciated. This work was supported by a NSF Postdoctoral Research Fellowship and NSF grant EAR-0087463 to J.E.H.

References

Albarede, F., and A. Provost, Petrologic and geochemical mass-balance equations: An algorithm for least-squares fitting and general error analysis, *Comput. Geosci.*, *3*, 309–326, 1977.

Armienti, P., M. T. Pareschi, F. Innocenti, and M. Pompilio, Effects of magma storage and ascent on the kinetics of crystal growth—The case of the 1991–93 Mt Etna eruption, *Contrib. Mineral. Petrol.*, *115*, 402–414, 1994.

Avrami, M., Kinetics of phase change, I, *J. Chem. Phys.*, *7*, 1103–1112, 1939.

Avrami, M., Kinetics of phase change, II, *J. Chem. Phys.*, *8*, 212–224, 1940.

Barclay, J., M. J. Rutherford, M. R. Carroll, M. D. Murphy, J. D. Devine, J. Gardner, and R. S. J. Sparks, Experimental phase equilibria constraints on pre-eruptive storage conditions of the Soufriere Hills magma, *Geophys. Res. Lett.*, *25*, 3437–3440, 1998.

Berkebile, C. A., and E. Dowty, Nucleation in laboratory charges of basaltic composition, *Am. Mineral.*, *67*, 886–899, 1982.

Blundy, J., and K. Cashman, Ascent-driven crystallisation of dacite magmas at Mount St Helens, 1980–1986, *Contrib. Mineral. Petrol.*, *140*, 631–650, 2001.

Brandeis, G., and C. Jaupart, Crystal sizes in intrusions of different dimensions; constraints on the cooling regime and the crystallization kinetics, in *Magmatic Processes: Physicochemical Principles*, edited by B. O. Mysen, *Spec. Publ. Geochem. Soc.*, *1*, 307–318, 1987.

Carslaw, H. S., and J. C. Jaeger, *Conduction of Heat in Solids*, 510 pp., Clarendon, Oxford, England, 1986.

Cashman, K., and J. Blundy, Degassing and crystallization of ascending andesite and dacite, *Philos. Trans. R. Soc. London, Ser. A*, *358*, 1487–1513, 2000.

Cashman, K. V., Crystallization of Mount St. Helens 1980–1986 dacite: A quantitative textural approach, *Bull. Volcanol.*, *50*, 194–209, 1988.

Cashman, K. V., Groundmass crystallization of Mount St. Helens dacite, 1980–1986: A tool for interpreting shallow magmatic processes, *Contrib. Mineral. Petrol.*, *109*, 431–449, 1992.

Cashman, K. V., and B. D. Marsh, Crystal size distribution (CSD) in rocks and the kinetics and dynamics of crystallization, II, Makaopuhi lava lake, *Contrib. Mineral. Petrol.*, *99*, 292–305, 1988.

Cashman, K. V., C. Thornber, and J. P. Kauahikaua, Cooling and crystallization of lava in open channels, and the transition of Pahoehoe lava to ′a′a, *Bull. Volcanol.*, *61*, 306–323, 1999.

Cheng, H., and R. Lemlich, Errors in measurement of bubble size distribution in foam, *Ind. Eng. Chem. Fundam.*, *22*, 105–109, 1983.

Christian, J. W., *The Theory of Transformations in Metals and Alloys*, 973 pp., Pergamon, New York, 1965.

Corrigan, G. M., The crystal morphology of plagioclase feldspar produced during isothermal supercooling and constant rate cooling experiments, *Mineral. Mag.*, *46*, 433–439, 1982.

Crisp, J., K. V. Cashman, J. A. Bonini, S. B. Hougen, and D. C. Pieri, Crystallization history of the 1984 Mauna Loa lava flow, *J. Geophys. Res.*, *99*, 7177–7198, 1994.

Davis, M. J., and P. D. Ihinger, Influence of hydroxyl on glass transformation kinetics in lithium disilicate melt and a re-evaluation of structural relaxation in NBS 710 and 711, *J. Non Cryst. Solids*, *244*, 1–15, 1999.

Davis, M. J., P. D. Ihinger, and A. C. Lasaga, Influence of water on nucleation kinetics in silicate melt, *J. Non Cryst. Solids*, *219*, 62–69, 1997.

Devine, J. D., J. E. Gardner, H. P. Brack, G. D. Layne, and M. J. Rutherford, Comparison of microanalytical methods for estimating H_2O contents of silicic volcanic glasses, *Am. Mineral.*, *80*, 319–328, 1995.

Devine, J. D., M. J. Rutherford, and J. E. Gardner, Petrologic determination of ascent rates for the 1995–1997 Soufriere Hills Volcano andesitic magma, *Geophys. Res. Lett.*, *25*, 3673–3676, 1998.

Dowty, E., Crystal growth and nucleation theory, in *Physics of Magmatic Processes*, edited by R. Hargraves, pp. 487–551, Princeton Univ. Press, Princeton, N. J., 1980.

Evans, B. W., and B. Scaillet, The redox state of Pinatubo dacite and the ilmenite-hematite solvus, *Am. Mineral.*, *82*, 625–629, 1997.

Fenn, P. M., The nucleation and growth of alkali feldspar from hydrous melts, *Can. Mineral.*, *15*, 135–161, 1977.

Fokin, V. M., O. V. Potapov, C. R. Chinaglia, and E. D. Zanotto, The effect of pre-existing crystals on the crystallization kinetics of a soda-lime-silica glass: The courtyard phenomenon, *J. Non Cryst. Solids*, *258*, 180–186, 1999.

Gardner, C. A., K. V. Cashman, and C. A. Neal, Tephra-fall deposits from the 1992 eruption of Crater Peak, Alaska: Implications of clast textures for eruptive processes, *Bull. Volcanol.*, *59*, 537–555, 1998.

Gardner, J. E., S. Carey, M. J. Rutherford, and H. Sigurdsson, Petrologic diversity in Mount St. Helens dacites during the last 4,000 years: Implications for magma mixing, *Contrib. Mineral. Petrol.*, *119*, 224–238, 1995.

Geschwind, C. H., and M. J. Rutherford, Crystallization of microlites during magma ascent; the fluid mechanics of 1980–1986 eruptions at Mount St. Helens, *Bull. Volcanol.*, *57*, 356–370, 1995.

Granasy, L., and P. F. James, Nucleation in oxide glasses: comparison of theory and experiment, *Proc. R. Soc. London, Ser. A*, *454*, 1745–1766, 1998.

Hammer, J. E., K. V. Cashman, and B. Voight, Magmatic processes revealed by textural and compositional trends in Merapi dome lavas, *J. Volcanol. Geotherm. Res.*, *100*, 165–192, 1998.

Hammer, J. E., K. V. Cashman, R. P. Hoblitt, and S. Newman, Degassing and microlite crystallization during pre-climactic events of the 1991 eruption of Mt. Pinatubo, Philippines, *Bull. Volcanol.*, *60*, 355–380, 1999.

Hammer, J. E., K. V. Cashman, and B. Voight, Magmatic processes revealed by textural and compositional trends in Merapi dome lavas, *J. Volcanol. Geotherm. Res.*, *100*, 165–192, 2000.

Hess, K.-U., and D. B. Dingwell, Viscosities of hydrous leucogranitic melts: A non-Arrhenian model, *Am. Mineral.*, *81*, 1297–1300, 1996.

Higgins, M. D., Numerical modeling of crystal shapes in thin sections; estimation of crystal habit and true size, *Am. Mineral.*, *79*, 113–119, 1994.

Higgins, M. D., Crystal size distributions and other quantitative textural measurements in lavas and tuff from Egmont Volcano (Mt. Taranaki), New Zealand, *Bull. Volcanol.*, *58*, 194–204, 1996a.

Higgins, M. D., Magma dynamics beneath Kameni Volcano, Greece, as revealed by crystal size and shape measurements, *J. Volcanol. Geotherm. Res.*, *70*, 37–48, 1996b.

Hildreth, W. E., The compositionally zoned eruption of 1912 in the Valley of Ten Thousand Smokes, Katmai National Park, Alaska, *J. Volcanol. Geotherm. Res.*, *18*, 1–56, 1983.

Holtz, F., M. Pichavant, P. Barbey, and W. Johannes, Effects of H_2O on liquidus phase-relations in the haplogranite system at 2 and 5 kbar, *Am. Mineral.*, *77*, 1223–1241, 1992.

Hort, M., Cooling and crystallization in sheet-like magma bodies revisited, *J. Volcanol. Geotherm. Res.*, *76*, 297–317, 1997.

Hort, M., and T. Spohn, Crystallization calculations for a binary melt cooling at constant rates of heat removal: Implications for the crystallization of magma bodies, *Earth Planet. Sci. Lett.*, *107*, 463–474, 1991.

Jackson, K., Current concepts in crystal growth: The fundamental rate equation, *J. Crystal Growth*, *5*, 13–18, 1969.

James, P. F., Nucleation in glass-forming systems—A review, in *Advances in Ceramics*, edited by J. H. Simmons, D. R. Uhlmann, and G. H. Beall, pp. 1–48, Am. Ceramic Soc., Columbus, Ohio, 1982.

James, R., and D. Hamilton, Phase relations in the system $NaAlSi_3O_8$-$KAlSi_3O_8$-$CaAl_2Si_2O_8$-SiO_2-H_2O at 1 kb water vapor pressure, *Contrib. Mineral. Petrol.*, *21*, 111–141, 1969.

Johannes, W., Beginning of melting in the granite system Qz-Ab-Or-An-H_2O, *Contrib. Mineral. Petrol.*, *84*, 264–273, 1984.

Johannes, W., and F. Holtz, *Petrogenesis and Experimental Petrology of Granitic Rocks*, 335 pp., Springer-Verlag, New York, 1996.

Johnson, W., and R. Mehl, Reaction kinetics in processes of nucleation and growth, *Am. Inst. Min. Eng.*, *1089*, 1–27, 1939.

Kirkpatrick, R. J., Kinetics of crystallization of igneous rocks, in *Kinetics of Geochemical Processes*, *Rev. Mineral.*, vol. 8, edited by A. C. Lasaga and R. J. Kirkpatrick, pp. 321–397, Mineral. Soc. of Am., Washington, D. C., 1981.

Kirkpatrick, R. J., G. R. Robinson, and J. F. Hays, Kinetics of crystal growth from silicate melts: Anorthite and diopside, *J. Geophys. Res.*, *81*, 5715–5720, 1976.

Kirkpatrick, R. J., L. Klein, D. R. Uhlmann, and J. F. Hays, Rates and processes of crystal growth in the system anorthite-albite, *J. Geophys. Res.*, *84*, 3671–3676, 1979.

Klein, L., and D. R. Uhlmann, Crystallization behavior of anorthite, *J. Geophys. Res.*, *79*, 4869–4874, 1974.

Klug, C., and K. V. Cashman, Vesiculation of May 18, 1980, Mount St. Helens magma, *Geology*, *22*, 468–472, 1994.

Kouchi, A., A. Tsuchiyama, and I. Sunagawa, Effect of stirring on crystallization kinetics of basalt; texture and element partitioning, *Contrib. Mineral. Petrol.*, *93*, 429–438, 1986.

Kuritani, T., Phenocryst crystallization during ascent of alkali basalt magma at Rishiri Volcano, northern Japan, *J. Volcanol. Geotherm. Res.*, *88*, 77–97, 1999.

Lipman, P., D. Norton, J. J. Taggart, E. Brandt, and E. Engleman, Compositional variations in 1980 magmatic deposits, in *The 1980 Eruptions of Mount St. Helens, Washington*, edited by P. Lipman and D. Mullineaux, *U.S. Geol. Surv. Prof. Pap.*, *1250*, 631–640, 1981.

Lofgren, G., An experimental study of plagioclase crystal morphology: Isothermal crystallization, *Am. J. Sci.*, *274*, 243–273, 1974.

Lofgren, G. E., Experimental studies on the dynamic crystallization of silicate melts, in *Physics of Magmatic Processes*, edited by R. Hargraves, pp. 487–551, Princeton Univ. Press, Princeton, N. J., 1980.

Mangan, M. T., Crystal size distribution systematics and the determination of magma storage times: The 1959 eruption of Kilauea Volcano, Hawaii, *J. Volcanol. Geotherm. Res.*, *44*, 295–302, 1990.

Marsh, B. D., On the crystallinity, probability of occurrence, and rheology of lava and magmas, *Contrib. Mineral. Petrol.*, *78*, 85–98, 1981.

McCoy, T. J., and G. E. Lofgren, Crystallization of the Zagami shergottite: An experimental study, *Earth Planet. Sci. Lett.*, *173*, 397–411, 1999.

Melnik, O., and R. S. J. Sparks, Nonlinear dynamics of lava dome extrusion, *Nature*, *402*, 37–41, 1999.

Metrich, N., and M. J. Rutherford, Low pressure crystallization paths of H_2O-saturated basaltic-hawaiitic melts from Mt Etna: Implications for open-system degassing of basaltic volcanoes, *Geochim. Cosmochim. Acta*, *62*, 1195–1205, 1998.

Moore, G., T. Vennemann, and I. S. E. Carmichael, Solubility of water in magmas to 2 kbar, *Geology*, *23*, 1099–1102, 1995.

Morgan, G. B. V., and D. London, Optimizing the electron microprobe analysis of hydrous alkali aluminosilicate glasses, *Am. Mineral.*, *81*, 1176–1185, 1996.

Mourtada-Bonnefoi, C. C., A. Provost, and F. Albarede, Thermochemical dynamics of magma chambers: A simple model, *J. Geophys. Res.*, *104*, 7103–7115, 1999.

Muncill, G. E., and A. C. Lasaga, Crystal-growth kinetics of plagioclase in igneous systems: One atmosphere experiments and application of a simplified growth model, *Am. Mineral.*, *72*, 299–311, 1987.

Muncill, G. E., and A. C. Lasaga, Crystal-growth kinetics of plagioclase in igneous systems: Isothermal H_2O-saturated experiments and extension of a growth model to complex silicate melts, *Am. Mineral.*, *73*, 982–992, 1988.

Nakada, S., and Y. Motomura, Petrology of the 1991–1995 eruption at Unzen: Effusion pulsation and groundmass crystallization, *J. Volcanol. Geotherm. Res.*, *89*, 173–196, 1999.

Nakada, S., Y. Miyake, H. Sato, O. Oshima, and A. Fujinawa, Endogenous growth of dacite dome at Unzen Volcano (Japan), 1993–1994, *Geology*, *23*, 157–160, 1995.

Nekvasil, H., Ternary feldspar crystallization in high-temperature felsic magmas, *Am. Mineral.*, *77*, 592–604, 1992.

Nielsen, C., and H. Sigurdsson, Quantitative methods of electron microprobe analysis of sodium in natural and synthetic glasses, *Am. Mineral.*, *66*, 547–552, 1981.

Ohnenstetter, D., and W. L. Brown, Overgrowth textures, disequilibrium zoning, and cooling history of a glassy 4-pyroxene boninite dyke from New-Caledonia, *J. Petrol.*, *33*, 231–271, 1992.

Pallister, J. S., R. P. Hoblitt, G. P. Meeker, R. J. Knight, and D. F. Siems, Magma mixing at Mount Pinatubo: Petrographic and chemical evidence from the 1991 deposits, in *Fire and Mud: Eruptions and Lahars of Mount Pinatubo, Philippines*, edited by C. G. Newhall and R. S. Punongbayan, pp. 687–732, Univ. of Wash. Press, Seattle, 1996.

Papale, P., and F. Dobran, Magma flow along the volcanic conduit during the Plinian and pyroclastic flow phases of the May 18, 1980, Mount St. Helens eruption, *J. Geophys. Res.*, *99*, 4355–4373, 1994.

Petersen, J. S., and G. E. Lofgren, Lamellar and patchy intergrowths in feldspars: Experimental crystallization of eutectic silicates, *Am. Mineral.*, *71*, 343–355, 1986.

Peterson, T. D., A refined technique for measuring crystal size distributions in thin section, *Contrib. Mineral. Petrol.*, *124*, 395–405, 1996.

Polacci, M., P. Papale, and M. Rosi, Textural heterogeneities in pumices from the climactic eruption of Mount Pinatubo, 15 June 1991, and implications for magma ascent dynamics, *Bull. Volcanol.*, *63*, 83–97, 2001.

Porter, D., and K. Easterling, *Phase Transformations in Metals and Alloys*, 514 pp., Chapman and Hall, New York, 1997.

Pownceby, M. I., and H. S. C. O'Neill, Thermodynamic data from redox reactions at high-temperatures, 4, Calibration of the Re-ReO_2 oxygen buffer from Emf and NiO + Ni-Pd redox sensor measurements, *Contrib. Mineral. Petrol.*, *118*, 130–137, 1994.

Putnis, A., *Introduction to Mineral Sciences*, 457 pp., Cambridge Univ. Press, New York, 1992.

Resmini, R. G., and B. D. Marsh, Steady-state volcanism, paleoeffusion rates, and magma system volume inferred from plagioclase crystal size distributions in mafic lavas: Dome Mountain, Nevada, *J. Volcanol. Geotherm. Res.*, *68*, 273–296, 1995.

Roselle, G. T., L. P. Baumgartner, and J. A. Chapman, Nucleation-dominated crystallization of forsterite in the Ubehebe peak contact aureole, California, *Geology*, *25*, 823–826, 1997.

Rutherford, M., and J. Devine, Changing magma conditions and ascent rates during the Soufriere Hills eruption on Montserrat, *GSA Today*, *8*, 1–7, 1997.

Rutherford, M. J., and J. D. Devine, Pre-eruption pressure-temperature conditions and volatiles in the 1991 dacitic magma of Mount Pinatubo, in *Fire and Mud: Eruptions and Lahars of Mount Pinatubo, Philippines*, edited by C. Newhall and R. Punongbayan, pp. 751–766, Univ. of Wash. Press, Seattle, 1996.

Rutherford, M. J., and J. E. Gardner, Rates of magma ascent, in *Encyclopedia of Volcanoes*, edited by H. S. Sigurdsson, pp. 207–218, Academic, San Diego, Calif., 2000.

Rutherford, M. J., and P. M. Hill, Magma ascent rates from amphibole breakdown: An experimental study applied to the 1980–1986 Mount St. Helens eruptions, *J. Geophys. Res.*, *98*, 19,667–19,685, 1993.

Sahagian, D., and A. Proussevitch, Thermal effects of magma degassing, *J. Volcanol. Geotherm. Res.*, *74*, 19–38, 1996.

Simakin, A., V. Trubitsyn, and H. Schmeling, Structure of the upper boundary-layer of a solidifying intrusion with crystal sedimentation, *Earth Planet. Sci. Lett.*, *126*, 333–349, 1994.

Smith, J., and W. Brown, *Feldspar Minerals,* vol. 1, *Crystal Structures, Physical, Chemical, and Microtextural Properties*, 828 pp., Springer-Verlag, New York, 1988.

Solomatov, V. S., and D. J. Stevenson, Kinetics of crystal growth in a terrestrial magma ocean, *J. Geophys. Res.*, *98*, 5407–5418, 1993.

Sparks, R. S. J., Causes and consequences of pressurisation in lava dome eruptions, *Earth Planet. Sci. Lett.*, *150*, 177–189, 1997.

Stewart, D., and E. Roseboom, Lower temperature termination of the three-phase region plagioclase-alkali feldspar-liquid, *J. Petrol.*, *3*, 280–315, 1962.

Stix, J., et. al., A model of degassing at Galeras Volcano, Colombia, 1988–1993, *Geology*, *21*, 963–967, 1993.

Swanson, S. E., Relation of nucleation and crystal-growth rate to the development of granitic textures, *Am. Mineral.*, *62*, 966–978, 1977.

Swanson, S. E., and P. M. Fenn, Quartz crystallization in igneous rocks, *Am. Mineral.*, *71*, 331–342, 1986.

Swanson, S. E., M. T. Naney, H. R. Westrich, and J. C. Eichelberger, Crystallization history of Obsidian Dome, Inyo Domes, California, *Bull. Volcanol.*, *51*, 161–176, 1989.

Tammann, G., and R. Mehl, *The States of Aggregation*, 297 pp., Van Nostrand Reinhold, New York, 1925.

Toramaru, A., A numerical experiment of crystallization for a binary eutectic system with application to igneous textures, *J. Geophys. Res.*, *106*, 4037–4060, 2001.

Tuttle, O., and N. Bowen, *Origin of Granite in Light of Experimental Studies*, 153 pp., Geol. Soc. of Am., Boulder, Colo., 1958.

Venezky, D. Y., and M. J. Rutherford, Preeruption conditions and timing of dacite-andesite magma mixing in the 2.2 ka eruption at Mount Rainier, *J. Geophys. Res.*, *102*, 20,069–20,086, 1997.

Voight, B., et. al., Magma flow instability and cyclic activity at Soufriere Hills Volcano, Montserrat, British West Indies, *Science*, *283*, 1138–1142, 1999.

Watson, I. M., et. al., The relationship between degassing and ground deformation at Soufriere Hills Volcano, Montserrat, *J. Volcanol. Geotherm. Res.*, *98*, 117–126, 2000.

Westrich, H. R., H. W. Stockman, and J. C. Eichelberger, Degassing of rhyolitic magma during ascent and emplacement, *J. Geophys. Res.*, *93*, 6503–6511, 1988.

Whitney, J., The origin of granite: The role and source of water in the evolution of granitic magmas, *Geol. Soc. Am. Bull.*, *100*, 1886–1897, 1988.

Wilson, L., R. S. J. Sparks, and G. P. L. Walker, Explosive volcanic eruptions, IV, The control of magma properties and conduit geometry on eruption column behaviour, *Geophys. J. R. Astron. Soc.*, *63*, 117–148, 1980.

Wolf, K. J., and J. C. Eichelberger, Syneruptive mixing, degassing, and crystallization at Redoubt Volcano, eruption of December, 1989 to May 1990, *J. Volcanol. Geotherm. Res.*, *75*, 19–38, 1997.

Zanotto, E. D., and M. L. G. Leite, The nucleation mechanism of lithium dissilicate glass revisited, *J. Non Cryst. Solids*, *202*, 145–152, 1996.

J. E. Hammer and M. J. Rutherford, Department of Geological Sciences, Brown University, P.O. Box 1846, Providence, RI 02912-1846, USA. (jhammer@brown.edu)